Light-fuelled primitive replication and selection in evolvable biomimetic chemical networks

Éva Bartus[a,b], Attila Tököli[a], Beáta Mag[a], Áron Bajcsi[a], Gábor Kecskeméti[a], Edit Wéber[a], Zoltán Kele[a], Gabriel Fenteany[a,c], Tamás A. Martinek[a,b]*

[a] É. Bartus, A. Tököli, B. Mag, Á. Bajcsi, G. Kecskeméti, E. Wéber, Z. Kele, T. A. Martinek
Department of Medical Chemistry
University of Szeged
Dóm tér 8, H-6720 Szeged, Hungary
E-mail: martinek.tamas@med.u-szeged.hu
[b] É. Bartus, T. A. Martinek
MTA-SZTE Biomimetic Systems Research Group
University of Szeged
Dóm tér 8, H-6720 Szeged, Hungary
[c] G. Fenteany
Institute of Genetics
Biological Research Centre
Temesvári krt. 62, H-6726 Szeged, Hungary

Abstract: The concept of chemically evolvable replicators is central to abiogenesis. Evolvability requires three essential components: energy harvesting mechanisms for non-equilibrium dissipation, kinetically asymmetric decomposition pathways, and transfer of structural information in the autocatalytic cycles. We observed a UVA light-fuelled chemical network displaying sequence-dependent replication and replicator decomposition. The system was constructed with primitive peptidic foldamer components. The photocatalytic formation-recombination cycle of thiyl radicals was coupled with the molecular recognition steps in the replication cycles. Thiyl radical-mediated chain reaction was responsible for the replicator death mechanism. The competing and kinetically asymmetric replication and decomposition processes led to light intensity-dependent selection far from equilibrium. Here we show that this system can dynamically adapt to the level of energy influx and seeding. The results highlight the feasibility of the complex phenomenon of chemical evolvability with primitive building blocks and simple chemical reactions.

Introduction

Chemical networks mimicking evolution need to operate dynamically far from equilibrium[1], which is essential for their open-ended adaptive behaviour. The dynamic kinetic stability in such systems results from the balance between the asymmetric formation and destruction processes driven by the dissipation of energy harvested from the environment[2]. Besides metabolism and compartmentalisation, dissipative replication and selection are crucial components for modelling chemical evolution. Non-equilibrium dynamics occur in dissipative chemical networks[2a, 3], which rely on an energy-harvesting catalytic cycle covering the entropy production of the system. Engineered dissipative systems[2b, 4] attain off-equilibrium states present in the non-covalent assembly of the building blocks[5]. The dissipative self-organisation of material can be a source of structural complexity[6] linked to the emergence of life.

Chemical[6c, 7] or light energy[8] can promote chemical replication by producing precursors in a protometabolic manner. However, a current challenge is driving replication and replicator decomposition simultaneously with external energy. Our goal was to find a feasible energy-harvesting covalent chemistry that drives both synthetic and breakdown processes asymmetrically depending on the intensity of the energy influx. UV-induced photochemical rearrangement reactions can be carried out with aliphatic disulfides in the organic liquid phase[9] and an aqueous medium.[10] These works showed that both UVA and UVB induce photolysis, producing thiyl radicals despite the strongly reduced absorbance of the disulfide group in the UVA region[9b, 10c]. Thiyl radicals participate in a diffusion-controlled chain reaction, and depending on the steric accessibility, the exchange proceeds through radical substitution or recombination. Strikingly, anomalously high reaction rates were obtained for the bulky *iso*-butyl substituent,[9a] indicating that the reaction is not always governed by the diffusion-controlled collision of the thiyl radicals. These seminal findings suggest that photochemical disulfide rearrangement facilitates both diffusion-controlled and proximity-controlled mechanisms in a substituent-dependent manner. Since these kinetically asymmetric mechanisms are of different order functions of light intensity (see below), they promise an energy-dependent response, potentially paving the way toward dissipative behaviour.

We set out to test the photochemical disulfide rearrangement with a diverse population of helical foldamers as substituents in the aqueous medium. In order to avoid rapid decomposition of the peptidic chains, the feasibility of the light-induced disulfide rearrangement was investigated at UVA wavelengths. We hypothesised that preferential binding between the foldamer chains could exert side chain-dependent proximity control over the photochemical exchange. In contrast, non-interacting segments should readily enter the diffusion-governed chain reaction. The competition between the two processes was expected to yield a light intensity-dependent composition without damaging the peptidic chains. Seeking potential autocatalytic phenomena, we aimed to investigate the influence of the foldamer-foldamer interactions on the energy-harvesting thiyl chemistry. Designed helical peptides can transfer structural information in autocatalytic processes[11], and exponential replication has been achieved for peptidic helices[12]. Helical foldamers are excellent models because the folding can be readily controlled to generate the biomimetic recognition surface[13]. Moreover, short peptidomimetic foldamers can self-associate in solution[14], which is an advantageous feature in terms of proximity control.

Here, we show that UVA light-fuelled disulfide rearrangement can drive a chemical network to off-equilibrium states in a dissipative

manner. We found that sequence-dependent auto-/cross-catalysis plays dominant role in the exchange processes facilitating replication. A competing break down mechanism influenced the replicator concentration and thereby laid the foundation for the adaptive selection phenomenon.

Results

The UVA-induced photochemical disulfide rearrangement is feasible in a foldamer library. We constructed the foldamer library using hexameric β-peptide foldamers designed to fold into compact helical structures[15] (Figure 1a). The sequences contained two variable positions (Xaa^1 and Xaa^2), where proteinogenic side chains were incorporated. These can successfully probe protein surfaces[13a], and the ordered secondary structure can promote self-association[14]. We did not pursue other designs to keep the complexity of the sequences at a low level. Cys residues were attached to the C-terminus, which allowed for disulfide linkage between two foldamer segments yielding dimers (Figure 1a). We define the disulfides containing only one foldamer and glutathione as monomers.

Before the photochemical experiments, the sequence-dependent association tendency of the foldamer segments was validated in an aqueous glutathione redox buffer by relaxing the system to equilibrium with the dynamic covalent thiolate mechanism (Figure S1a). In equilibrium, this setup yielded 78 different dimers and 12 monomers (Table S1), and the product distribution was biased toward the hydrophobic dimers indicating sequence-dependent association.

For the photochemical exchange experiments, the presence of free thiol groups was eliminated, and the pH was set to 7.0 to block the light-independent thiolate-mediated nucleophilic disulfide exchange. It was essential to avoid the rapid degradation of the peptidic chains; therefore, the disulfide rearrangement reactions were attempted driven by UVA irradiation (365 nm) at constant temperature (303 K) according to literature protocols[10c]. First, we tested the UVA-induced break down of the dimers (10 μM each) to monomers in the presence of oxidised glutathione (500 μM). In this step, the starting dimers were synthesised by using a limited set of foldameric segments: **RW, WF, LW,** and **TW**, allowing ten different combinations. One-letter codes correspond to the variable side chains in the standard α-amino acid notation. The UVA illumination at 5.1 mW cm^{-1} decreased the dimer concentrations, while monomers were produced in a time-dependent manner (Figure 1b and S2a). Second, we started the reaction from the monomer mixture **RW-G**, **WF-G, LW-G,** and **TW-G**, and the results confirmed the UVA-induced synthesis of dimers and the parallel decay of the monomer concentration (Figure 1c and S2b).

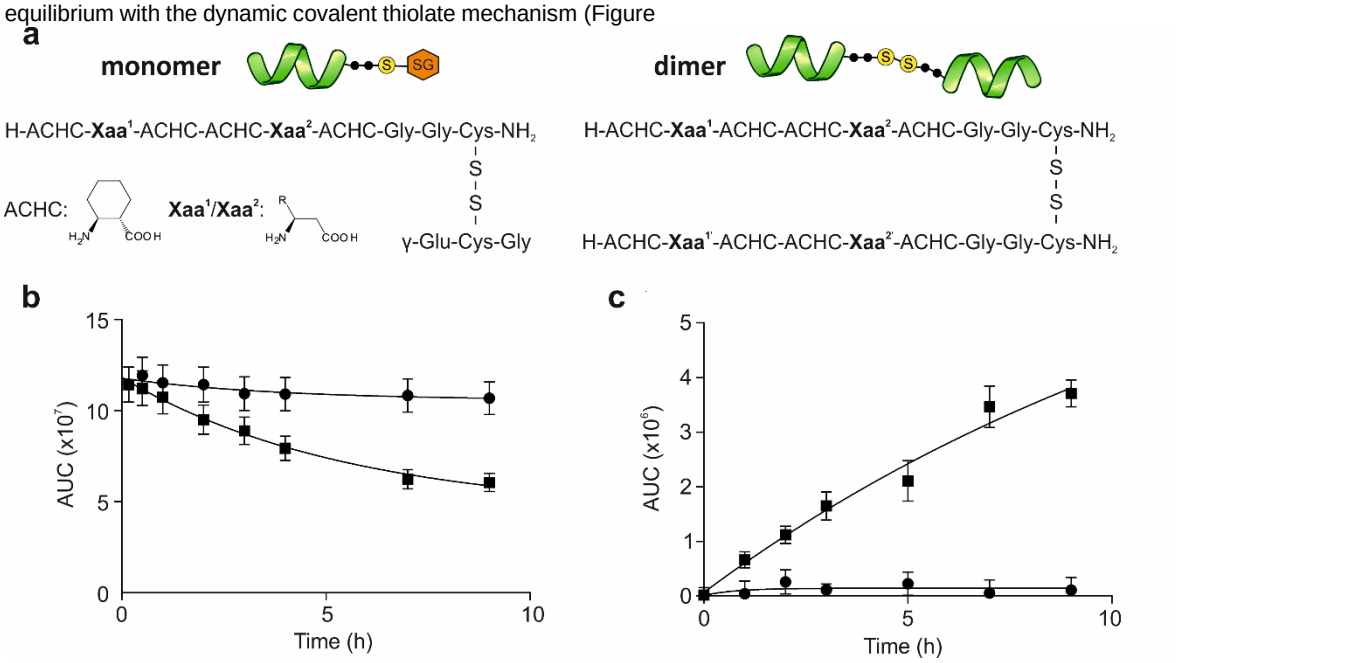

Figure 1. General sequences of the foldamer disulfide components and their synthesis and break down in the photochemical disulfide-exchange reaction. (**a**) SG indicates the glutathione (γ-L-glutamyl-L-cysteinyl-glycine), and ACHC stands for 1*S*,2*S*-2-aminocyclohexanecarboxylic acid, which promotes helical folding. In the highlighted positions Xaa^1 and Xaa^2, β^3-amino acids with proteinogenic side chains were incorporated in the following combinations: **IF, KW**, **LW, QW, RW, RF, SW, TW, VW, WF, WW,** and **YF**. One-letter codes correspond to the side chains in the standard α-amino acid notation. **b**) Concentration decay of the **RW-RW** dimer as a result of UVA irradiation at 365 nm (square) and without UVA illumination (circle). This reaction was started with a system containing all 10 dimers formed by combining the subset **RW, WF, LW,** and **TW**. Dimer concentrations were 10 μM for each combination. The system also contained 500 μM oxidised glutathione. In parallel, the amount of monomer (**RW-G**) increases at the expense of **RW**-containing dimers without the formation of undesired side products (Figure S2) **c**) Time-dependent concentration increase of the **RW-RW** dimer as a result of UVA irradiation at 356 nm (square) and without UVA (circle). This experiment was started with pure monomers of **RW-G, WF-G**, **LW-G,** and **TW-G**.

Degradation of the peptides was not observed during the experiments. We found no conversion without UVA illumination, and nitric oxide blocked the photocatalytic reaction. These observations confirmed the literature findings that the exchange reaction could be induced with UVA light centred at 365 nm, and it proceeds *via* a radical mechanism.

The UVA-dependent reaction contrasts with the absorbance maximum of the disulfide bond at around 280 nm[16]. However, a recent work showed that conformation-dependent stereoelectronic effects around the S-S bond could shift the absorption to the UVA region[17]. To test this phenomenon, we measured a simple disulfide model, cystamine, which displayed a concentration-dependent absorption tail in the UVA region (Figure S1b). A representative monomer **RW-G** was also tested, and the absorption tail was observed in the 330 – 400 nm range. In line with the literature, these findings strongly supported the ability of the disulfide group to absorb light energy at around 365 nm and thus, drive the photochemical rearrangement. We concluded that UVA illumination facilitated monomer - dimer conversion in both directions: dimer synthesis and break down.

Light intensity- and sequence-dependent kinetic asymmetry in the photochemical foldamer-disulfide exchange.

In the next step, we tested the photocatalytic disulfide exchange on a larger library of pure monomers. We chose 12 different side chain combinations based on their tendency to self-associate and the ability to bind to hydrophobic patches[18]: **IF**, **KW**, **LW**, **QW**, **RW**, **RF**, **SW**, **TW**, **VW**, **WF**, **WW,** and **YF**. The power density was increased linearly in four steps up to the maximum value available in our setup (5.10 mW cm^{-2}). Without irradiation and at 25% light intensity, we could not detect dimer formation. At 50% and above, dimers were observed, and the system attained steady states at low conversions (without monomer depletion) in 5 h (Figure 2a and Figure S3-S4). The increasing light intensity caused the onset of a steep increase in the steady-state dimer population only above 4.0 mW/cm^2 (Figure 2b). This unexpected light intensity – concentration relationship could be mathematically approximated with a hyperbolic curve. We carried out a separate light intensity-dependent experiment, where the UVA intensity of 3.80 mW/cm^2 was applied first, and after reaching the corresponding stationary state, the intensity was increased to 4.80 mW/cm^2 for the same sample (Figure 2c). The dimer population again increased, and a new steady-state was attained adaptively. The light intensity-dependence of the steady-state dimer concentrations evidences competition between the break down and synthetic processes, which are of different order functions of the light intensity. This is possible only if the break down and the synthesis proceed *via* different light-induced mechanisms. Thus, an energy influx-dependent kinetic asymmetry determines the behaviour of the system.

We calculated the light-induced amplifications for the dimers upon elevating the power density from 2.55 mW/cm^2 (50%) to 5.10 mW cm^{-2} (100%) (Figure 2d). We found highly sequence-dependent amplification with more than two magnitudes difference between the best and the worst amplified dimers. For the set of the ten most populated sequences, enrichment of aromatic and aliphatic hydrophobic side chains was detected relative to the complete set of dimers (Figure 2e). In parallel, depletion of polar and cationic residues was measured at the peripheral positions (1 and 1´). We concluded that the kinetic asymmetry is highly sequence-dependent as well.

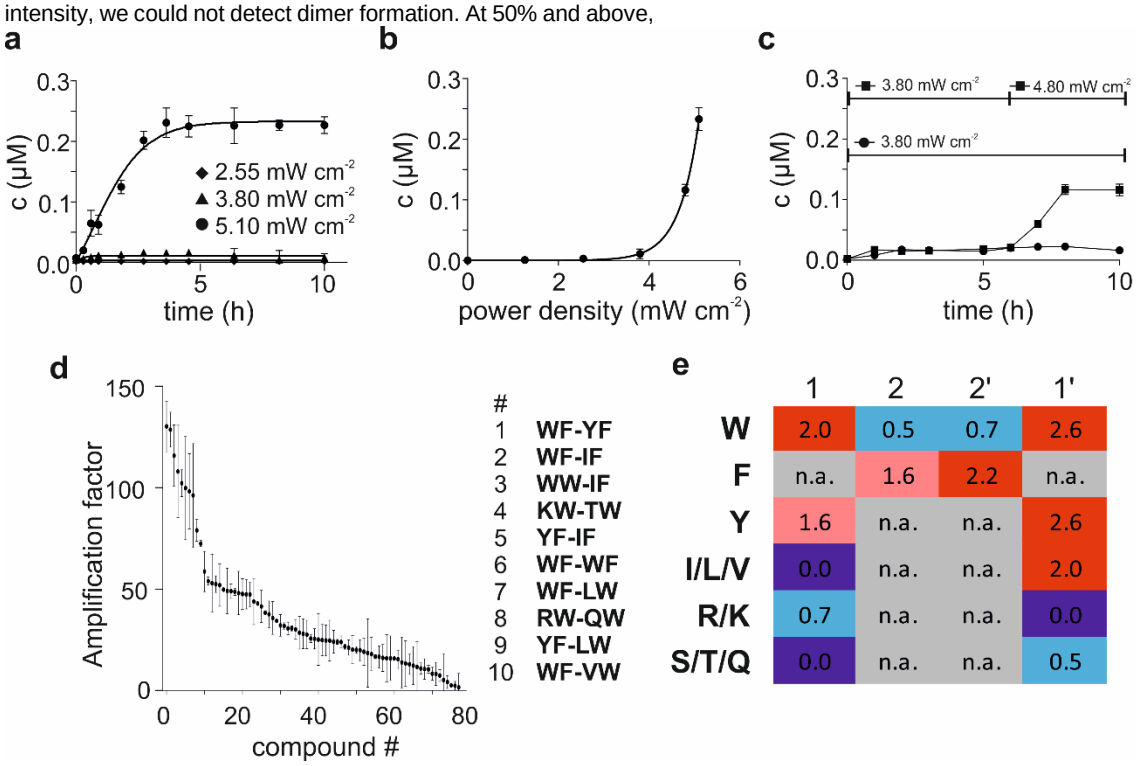

Figure 2. Light intensity- and substituent-dependent concentrations. (**a**) Time- and light intensity-dependent concentration of a representative dimer (**WF-YF**) obtained at power densities of 2.55 mW cm^{-2} (diamonds), 3.80 mW cm^{-2} (triangles), 5.10 mW cm^{-2} (circles). (**b**) Light intensity-dependent steady-state concentrations for **WF-YF** (circles). (**c**) The adaptivity test started with a UVA intensity of 3.80 mW cm^{-2} and subsequent increase to 4.80 mW cm^{-2} (squares), and the control measurement run with a constant intensity of 3.80 mW cm^{-2} (circles). (**d**) Light intensity-dependent amplifications obtained upon increasing power density from 2.55 mW cm^{-2} to 5.10 mW cm^{-2} with the ten most amplified sequences indicated (inset). (**e**) Side-chain enrichments in the peripheral (1, 1´) and the central (2, 2´) positions for the ten most amplified dimers (n.a. stands for 'not applicable').

Sequence-dependent auto- and cross-catalysis are present in the system. The hyperbolic relationship between the steady-state dimer concentrations and the light intensity was a striking feature that justified further investigations. For certain dimers, we observed a time delay in the synthesis curve, which suggested the presence of autocatalysis in the system (Figure 3b). We hypothesised that autocatalysis is coupled to the light-driven synthesis routes, which can be tested in the time-domain with a seeding experiment. The effective light-induced spontaneous seeding is inseparable from the auto-/cross-catalysis due to the low complexity of the building blocks. These pathways can successfully hide the autocatalytic time delay for many dimers, but an increase in the initial rate of the synthesis would be a clear indicator of the catalytic effect. However, the break down of a potential seeding dimer immediately starts upon UVA irradiation. Thus, we would not be able to prove that the seed is a catalyst, that is, not consumed in the reaction. To circumvent this problem, we synthesised a seeding dimer with an isosteric but light insensitive thioether coupling unit closely mimicking the best amplifying dimer **WF-YF** (**WF-S-YF**, Figure 3a). Seeding the mixture with **WF-S-YF** at a concentration of 10 μM led to a marked increase in the initial synthesis rates (measured at 40 min) (Figure 3b and 3c), while the seed concentration remained constant. This proved the catalytic effect of the seeding dimer. The parent dimer **WF-YF** displayed ca. four-fold increase in the initial rate (Figure 3d). This finding strongly supports the presence of autocatalysis in the system. The catalytic effect appeared for other sequences too, but the cross-catalysis was sequence-dependent. It tapered off steeply as the sequence similarity decreased. Even within this set of primitive structures with only two variable side chains, the catalytic interaction distinguishes the foldameric sequences. This experiment demonstrates the presence of sequence-dependent auto- and cross-catalysis in the system. Since the auto-/cross-catalysis is not possible without contact between the dimer products and the monomer precursors, templating and proximity have to play important roles in the catalytic step.

The amplification effect of the auto-/cross-catalysis explains the highly sequence-dependent selection observed in the light intensity-dependent experiment (Figure 2d). Dimers having an effective and large number of auto-/cross-catalytic interactions can be dominant at sufficient energy influx. The small size (< 1000 Da) and the low complexity of the foldameric segments do not afford a completely specific copy, but the highly sequence-dependent auto-/cross-catalytic amplification corresponds to a primitive form of chemical replication. The numeric analysis of the dynamic model (see below) independently proved that the hyperbolic light intensity response is explained by autocatalysis.

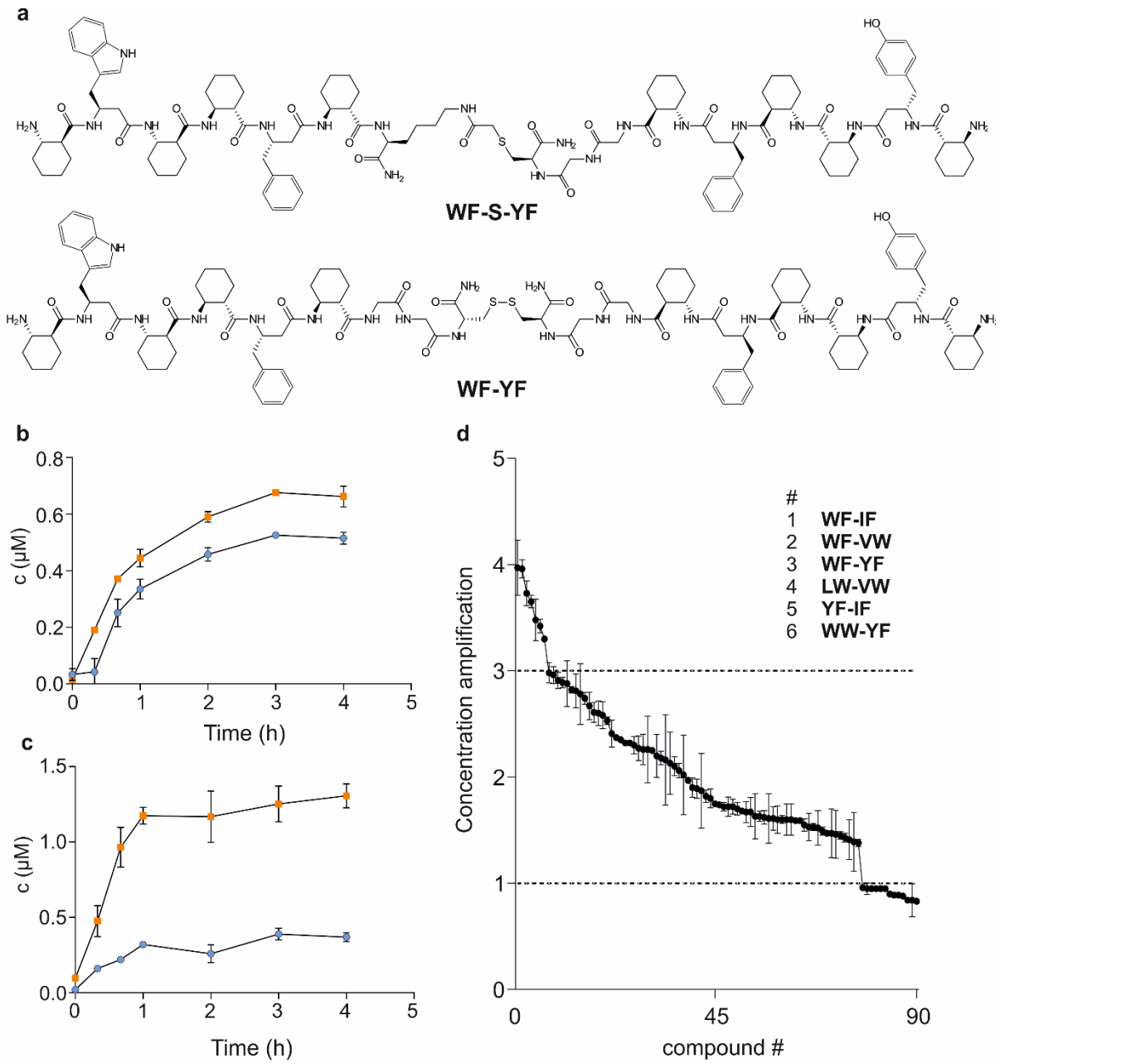

Figure 3. Catalytic effects of seeding with WF-S-YF. (**a**) Structure of the seeding dimer (**WF-S-YF**) with the light-insensitive thioether linkage and the structure of **WF-YF** dimer. Time evolution of the concentrations for representative dimers **RF-VW** (**b**) and **WF-IF** (**c**) with (orange square) and without (blue circle) the seeding dimer. Concentration amplifications ($c_{seeded}/c_{control}$) for the MSSM dimers upon seeding with **WF-S-YF** at 40 min (**d**) (Table S5).

Far-from-equilibrium dissipative adaptation.

The creation and maintenance of the various states observed for our system requires UVA irradiation as an external driving force. When the light is switched off after an illumination period, the system relaxes to a kinetic trap due to the absence of any microscopically reversible disulfide exchange mechanism. Here, the concentrations of the high-energy thiyl intermediates drop to zero, and the concentrations of the stable disulfide components get frozen at their instantaneous values. Without the continuous energy influx harvested and dissipated by the disulfide – thiyl conversion cycle, the system falls into a non-dissipative non-equilibrium state and loses its ability to adapt. On this ground, this system belongs to the class of dissipatively adapting non-equilibrium systems according to the literature definitions.[2c, 19] A number of published chemical dissipative structures,[5a, 6c, 20] relax to an attractor equilibrium when the external energy source is depleted or cut off providing an internal reference to measure the distance from equilibrium. In our system, the internal referencing is not feasible, but this feature does not make it non-dissipative until the UVA light is on. On the other hand, the thiolate-mediated equilibrium is a natural reference state for our system because it is governed by the binding affinity between the foldameric segments.

To estimate the distance of our system from this external reference equilibrium, we compared the photocatalytic dimer concentrations to the values obtained in equilibrium attained through the reversible thiolate-mediated exchange. We visualised the significant differences with the logarithm of the concentration ratios ($log(c_{Dissip}/c_{Equi})$) for each dimer and displayed the values on a heat map (Figure 4). At 75% light intensity, the steady-state dimer concentrations for the hydrophobic sequences are magnitudes below the equilibrium values (Figure 4a) due to the strong bias toward the decomposition mechanism. This finding shows that the system is far from the reference equilibrium already at low energy influx, but the break down process is predominant. This situation fundamentally changes at 100% light intensity because light-driven auto-/crosscatalysis successfully competes with the decomposition mechanism (Figure 4b). Hydrophobic sequences are still less favoured in the dissipative system, whereas dimers with polar or cationic side chains reach almost a magnitude higher concentrations relative to the reference equilibrium. The light intensity- and sequence-dependent magnitude level deviations from the reference demonstrate the ability of our system to adapt to the energy influx on a broad scale far from equilibrium.

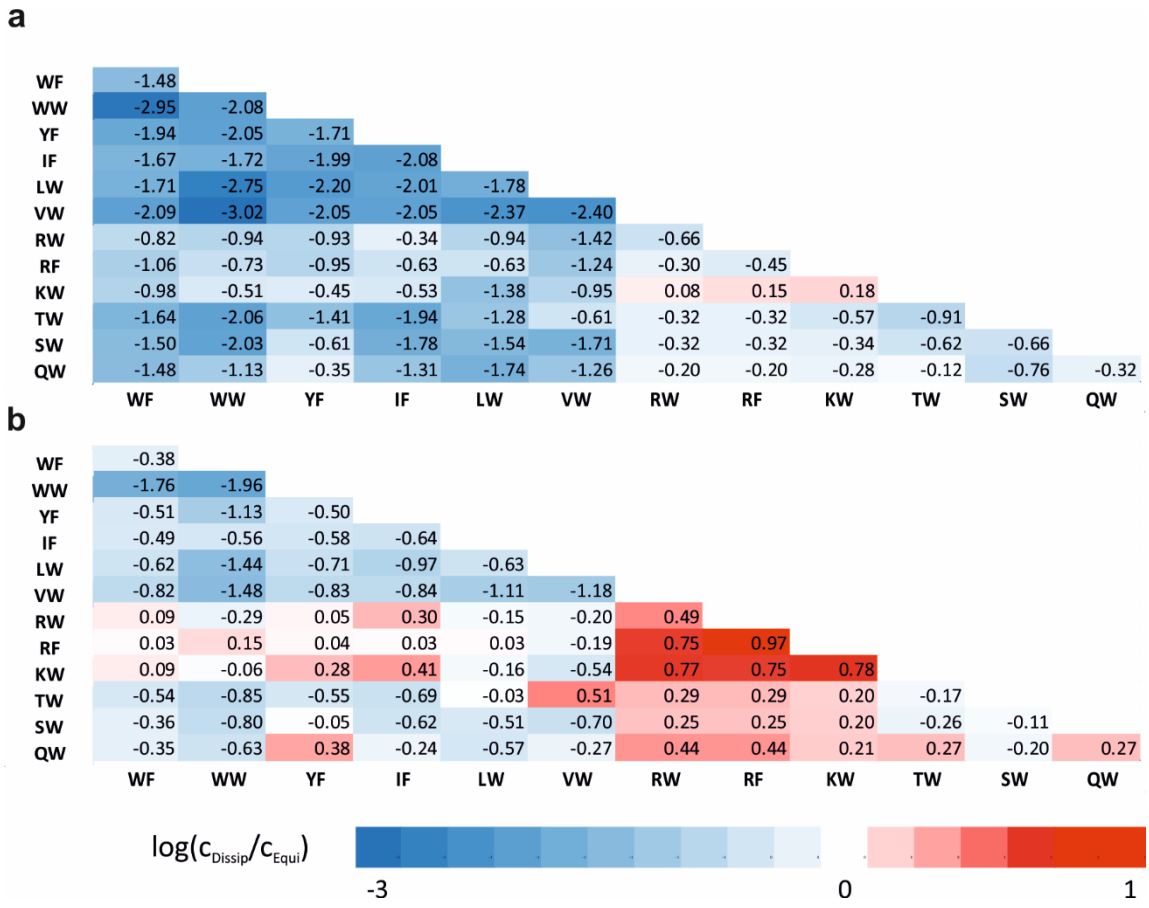

Figure 4. Light intensity- and sequence-dependent adaptation of the dimer concentrations relative to an external reference equilibrium. The logarithm of the concentration ratios ($log(c_{Dissip}/c_{Equi})$) is displayed on a heat map. c_{Dissip} stands for the steady-state concentrations measured in the kinetically asymmetric photochemical exchange at 75% light intensity (**a**) and 100% light intensity (**b**). c_{Equi} indicates the concentrations obtained in the thiolate-mediated exchange reaction relaxed to equilibrium. The combinations of monomers in the specific dimers are displayed as two-letter codes on the horizontal and vertical axes.

Dynamic model for the photocatalytic dissipative system. Dissipative systems out of the linear regime can only be handled within the framework of reaction kinetic models[2c]. Therefore, we propose here a dynamic model explaining the experimental findings. The light-induced thiyl radicals participate in a chain reaction as established in the literature[9a, 10b] (Figure 5a, [1]–[4]). In the absence of steric inhibition and preferential binding, the predominant exchange route is diffusion-controlled radical substitution (Figure 5a, [3] and [4]). Based on the preceding literature observation, the rate equations for dimer synthesis [3a] ($v_{s,ch}$) and breakdown [3b] (v_b) can be computed (eqs. (1) and (2)). The detailed calculations are provided in the Supplementary text.

$$v_{s,ch} = s_{ch}\sqrt{I}[\mathrm{MSSG}]^{1.5} \quad (1)$$

$$v_b = b\sqrt{I}[\mathrm{MSSM}] \quad (2)$$

The terms s_{ch} and b represent the corresponding rate constants, and I designates light intensity. Symbols [MSSG] and [MSSM] stand for the monomer and dimer concentrations, respectively. The central experimental finding of this work is that preferential binding (Figure 5c, [5]) facilitates the proximity-controlled exchange pathways. In this case, the light-induced homolytic cleavage [6] and the subsequent radical substitution [7] occur within the foldameric complexes. We cannot rule out *a priori* a

concerted metathesis with coincident absorption of two photons (Figure 5c, [8] and [9]). In this case, the cross-section of the interaction is not decreased by non-linear two-photon absorption effects because the two disulfides are separately excited. The corresponding rate equations for dimer formation via [7] ($v_{s,p1}$) and [9] ($v_{s,p2}$) can be derived through a binding preequilibrium and the rate-limiting intracomplex steps (eqs. (3) and (4)). See Supplementary text for the detailed computation.

$$v_{s,p1} = s_{p1} I [\mathrm{MSSG}]^2 \tag{3}$$

$$v_{s,p2} = s_{p2} I^2 [\mathrm{MSSG}]^2 \tag{4}$$

The proximity-controlled radical substitution and metathesis rate constants are s_{p1} and s_{p2}, respectively.

The light intensity-dependence of the steady-state concentration can be modelled with a hyperbolic curve, which can be obtained for this reaction system by incorporating autocatalysis into the model[21]. Indeed, we experimentally confirmed the presence of the auto/cross-catalysis (Figure 5f). This type of templating can exert autocatalysis on dimer formation by both proximity-controlled radical substitution (Figure 5e, [12]) and concerted disulfide metathesis (Figure 5c, [14]). The corresponding rate terms ($v_{s,a1}$ and $v_{s,a2}$) can be calculated (eqs. (6) and (7)). Details are provided in the Supplementary text.

$$v_{s,a1} = s_{a1} I [\mathrm{MSSM}][\mathrm{MSSG}]^2 \tag{6}$$

$$v_{s,a2} = s_{a2} I^2 [\mathrm{MSSM}][\mathrm{MSSG}]^2 \tag{7}$$

The autocatalytic radical substitution and concerted metathesis rate constants are s_{a1} and s_{a2}, respectively.

With eqs. (1)–(7), the steady-state concentration can be expressed (eq. (8)). However, we observed that the steady-state concentrations steeply converge to zero with decreasing light intensity for all sequences (Figure 2b). This result strongly suggests that the diffusion-controlled radical substitution (Figure 5a, [3a]) ($v_{s,ch}$) has no detectable contribution to the dimer synthesis ($s_{ch} \approx 0$); that is, the light-independent term is negligible in the numerator of eq. (8). Dimer synthesis, therefore, proceeds predominantly via the proximity-controlled pathways, whereas break down to monomers occurs through diffusion-controlled radical substitution. This observation simplifies eq. (8) to eq. (9).

$$[\mathrm{MSSM}]_{ss} = \frac{(s_{p1}\sqrt{I} + s_{p2} I^{1.5})[\mathrm{MSSG}]^2 + s_{ch}[\mathrm{MSSG}]^{1.5}}{b - (s_{a1}\sqrt{I} + s_{a2} I^{1.5})[\mathrm{MSSG}]^2} \tag{8}$$

$$[\mathrm{MSSM}]_{ss} = \frac{(s_{p1}\sqrt{I} + s_{p2} I^{1.5})[\mathrm{MSSG}]^2}{b - (s_{a1}\sqrt{I} + s_{a2} I^{1.5})[\mathrm{MSSG}]^2} \tag{9}$$

Thus, the light-intensity dependence also appears in the denominator explaining the hyperbolic function observed in the experiments. The hyperbolic approximation is valid only at low conversions ($[\mathrm{MG}] \approx [\mathrm{MG}]_0$), which holds for our experiments. Beyond the steady-state analysis, the dynamic model incorporating eqs. (2)–(7) was used to numerically simulate and fit the time- and light intensity-dependent data arrays with variable rate constants. Non-linear regressions were carried out simultaneously against all data points measured for the individual dimers. Excellent agreement was found (Figure 6a, solid curves and Figure S5). The regression against the dynamic model excluding the autocatalytic terms eqs. (6) and (7) failed (Figure 6a, dashed). Neither the hyperbolic response of the steady-state concentration nor the initial conversion rate changes upon the light intensity increase were captured correctly without the autocatalytic terms. This finding strongly supports that the hyperbolic response in the energy influx domain is a characteristic of autocatalysis. Together with the seeding results in the time-domain, we substantiated autocatalysis with two independent experiments.

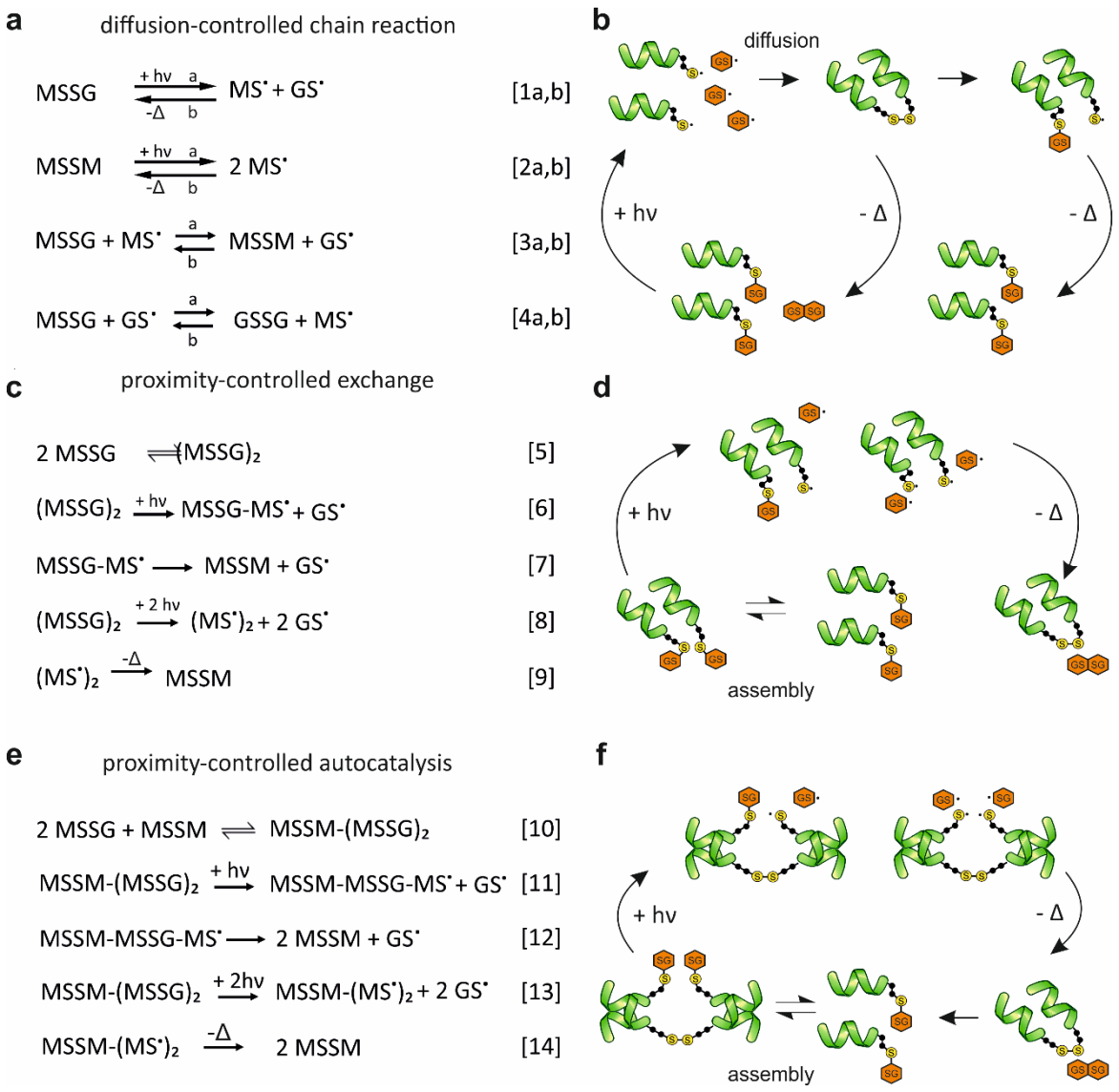

Figure 5. Steps of the photochemical disulfide-exchange mechanisms. A) Diffusion-controlled radical chain-reaction mechanism described in the literature for the photochemical disulfide exchange[9a]. The separate initiation ([1a] and [2a]), termination ([1b] and [2b]) and chain propagation steps ([3a,b] and [4a,b]) are indicated with the back-and-forth arrows, which do not refer to any preequilibrium or microscopic reversibility. **B**) Schematic representation of the replicator breakdown through diffusion-controlled radical substitution. **C**) The proximity-controlled reaction pathway with the foldamer association preequilibrium [5]. The intracomplex steps producing MSSM can be radical substitution ([7]) and concerted metathesis [9]. **D**) Spontaneous seeding *via* foldamer assembly and subsequent proximity-controlled radical substitution or concerted metathesis. **E**) The proposed proximity-controlled autocatalytic reaction mechanism. **F**) Templated cross-/autocatalysis facilitating the proximity-controlled radical substitution or concerted metathesis.

Time evolution of the reaction rates revealed that the autocatalytic pathway dominates dimer synthesis after 10 min (Figure 6b). The proximity-controlled, spontaneous (non-autocatalytic) mechanism is effective in seeding but would not produce detectable dimer formation within the observed time frame. Inspection of the resulting rate constants indicated that both the proximity-controlled radical substitution and the concerted metathesis mechanisms are present in the system. At the level of the individual dimers, however, the mechanism appeared dependent on the sequence (Table S2). Understanding this substituent-dependent mechanism requires further investigation, which is beyond the scope of the present work.

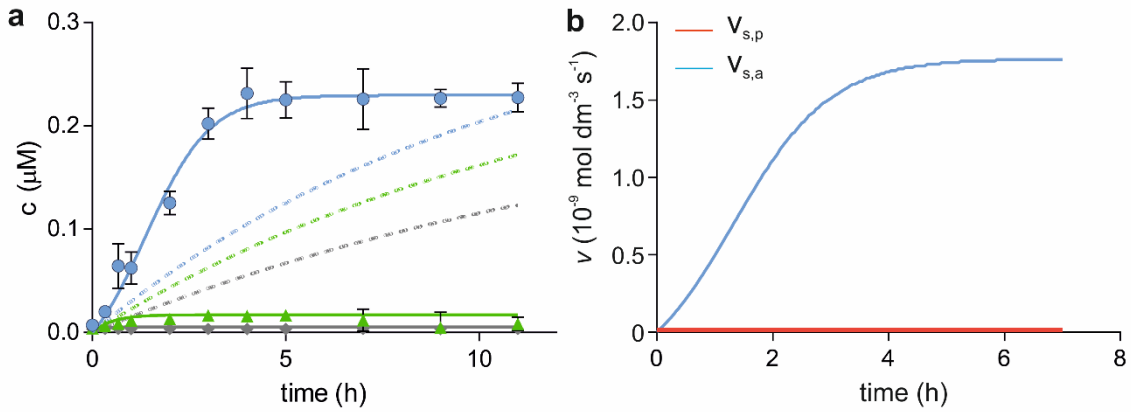

Figure 6. Non-linear regression of the dynamic model to the time- and light intensity-dependent data array and the effects of autocatalysis on dimer formation. A) The best-fitting dynamic models with (solid) and without (dashed curves) autocatalysis. Representative experimental time- and light intensity-dependent data array is shown for the dimer **WF-YF** measured at power densities of 2.55 mW cm^{-2} (grey), 3.80 mW cm^{-2} (green) and 5.10 mW cm^{-2} (blue). **B**) Time evolution of the reaction rates calculated for the proximity-controlled spontaneous synthesis ($v_{s,p}$: red) and the autocatalytic synthesis ($v_{s,a}$: blue) in the best-fitting dynamic model for **WF-YF**

Discussion

Disulfide linkage has a long history, and its nucleophilic exchange mechanism is currently popular in systems chemistry applications[22]. The photocatalytic rearrangement reaction of disulfides has also been known for decades.[9a] However, our work demonstrates the ability of the UV light-induced cleavage-recombination cycle of the disulfide bond to drive kinetically asymmetric processes. The root of asymmetry is the transient binding between peptidic segments that facilitates a fast intracomplex route for the thiyl-mediated exchange reactions under proximity control (Figure 5b). In parallel, the diffusion-controlled chain reaction in the background effectively couples disulfides with substituents that rapidly diffuse without preferential binding (Figure 5d). The weak interactions can exert proximity control because the high-energy radical intermediates rapidly relax to the dimer before entering the chain reaction. This finding suggests that the weak binding between primitive structures facilitates kinetic asymmetry if the dynamic covalent rearrangement is fast enough[23]. Since the competing mechanisms are affected by the light intensity in different orders, the light not only switched processes on and off, but the energy influx also influenced the extent of kinetic asymmetry. UVA irradiation drives the system to off-equilibrium steady states, ratcheting up the fittest sequences[2a, 24], and the system relaxes into a kinetic trap in dark. Thus, the system meets the criteria of dissipativity.

The modular nature of the foldameric disulfides allowed templating interactions between the dimers and the monomers. This interaction extends the proximity-controlled mechanism to an autocatalytic process, thereby facilitating a primitive replication (Figure 5c). The replication and the replicator death mechanisms asymmetrically compete without physical separation of the pathways[25]. In this system, the tendency toward assembly into structures of increased complexity is amplified by replication. In contrast, rapid diffusion – a property associated with low complexity – promotes decomposition. Thus, the dissipative adaptation[23b, 26] in the present system helps elucidate the chemical mechanisms of spontaneous emergence of complexity by selection. Pioneering experiments with dissipative self-assembling systems established the principles that govern chemical energy[27] or light-driven[28] trajectories to off-equilibrium states that generate spatial proximity-based order. Peptide-disulfides in the photochemical exchange reaction can be an additional valuable tool to study the dissipative self-organisation of simple building blocks.

Conclusion

We successfully coupled the light-harvesting thiyl radical chemistry with the molecular recognition processes occurring in a foldameric network. This system unexpectedly displayed a primitive replication mechanism, a kinetically asymmetric replicator death pathway, and dissipative adaptation to the external energy source and seeding. Although these features are essential for chemical evolution, prebiotic chemistry is beyond the scope of this study. However, the chemical availability of primitive Cys-containing peptides is supported by prebiotic Cys-catalysed amino acid and peptide synthesis[29]. These findings make thiyl radical-mediated dissipative replication of short, folding peptidic sequences an intriguing mechanism[30], potentially illuminating energetic aspects of the transition from prebiotic chemical networks to biotic evolution.

Acknowledgements

We thank Prof. Sijbren Otto (University of Groningen) for the suggestions to the experiments given in Figures 2c and 3. Dr. Miklós Erdélyi and Prof. Gábor Szabó (University of Szeged) are acknowledged for the calibration of the UV light source used for the measurements.

Competing interests

The authors declare no competing interests.

Data availability

All data is available in the main text or the supporting information. All data and materials used in the analysis are available to any researcher for purposes of reproducing or extending the analysis.

Funding

This research was funded by the National Research, Development and Innovation Office of Hungary, grant number GINOP-2.2.1-15-2016-00007 and NKFIA K134754. T.A.M. acknowledges support from the Hungarian Academy of Sciences LENDULET-Foldamer. Ministry of Human Capacities, Hungary grant 20391-3/2018/FEKUSTRAT is acknowledged.

Keywords: dissipative • replicator • system chemistry • foldamer • photochemistry

[1] P. Adamski, M. Eleveld, A. Sood, Á. Kun, A. Szilágyi, T. Czárán, E. Szathmáry, S. Otto, *Nat Rev Chem* **2020**, *4*, 386-403.

[2] a) G. Ragazzon, L. J. Prins, *Nat Nanotechnol* **2018**, *13*, 882-889; b) N. Singh, G. J. Formon, S. De Piccoli, T. M. Hermans, *Adv Mater* **2020**, *32*, 1906834; c) J. L. England, *Nat Nanotechnol* **2015**, *10*, 919-923.

[3] a) E. Mattia, S. Otto, *Nat Nanotechnol* **2015**, *10*, 111-119; b) S. A. P. van Rossum, M. Tena-Solsona, J. H. van Esch, R. Eelkema, J. Boekhoven, *Chem Soc Rev* **2017**, *46*, 5519-5535.

[4] B. Rieß, R. K. Grötsch, J. Boekhoven, *Chem* **2020**, *6*, 552-578.

[5] a) A. Sorrenti, J. Leira-Iglesias, A. Sato, T. M. Hermans, *Nat Commun* **2017**, *8*, 15899; b) M. Kathan, S. Hecht, *Chem Soc Rev* **2017**, *46*, 5536-5550; c) J. Nanda, B. Rubinov, D. Ivnitski, R. Mukherjee, E. Shtelman, Y. Motro, Y. Miller, N. Wagner, R. Cohen-Luria, G. Ashkenasy, *Nat Commun* **2017**, *8*, 434.

[6] a) L. N. Green, H. K. Subramanian, V. Mardanlou, J. Kim, R. F. Hariadi, E. Franco, *Nat Chem* **2019**, *11*, 510-520; b) Z. Liu, L.-F. Wu, J. Xu, C. Bonfio, D. A. Russell, J. D. Sutherland, *Nat Chem* **2020**, *12*, 1-6; c) S. M. Morrow, I. Colomer, S. P. Fletcher, *Nat Commun* **2019**, *10*, 1011.

[7] a) B. Liu, J. Wu, M. Geerts, O. Markovitch, C. G. Pappas, K. Liu, S. Otto, *Angew Chem Int Edit* **2022**, *134*, e202117605; b) S. Yang, G. Schaeffer, E. Mattia, O. Markovitch, K. Liu, A. S. Hussain, J. Ottelé, A. Sood, S. Otto, *Angew Chem Int Edit* **2021**, *60*, 11344-11349; c) I. Maity, N. Wagner, R. Mukherjee, D. Dev, E. Peacock-Lopez, R. Cohen-Luria, G. Ashkenasy, *Nat Commun* **2019**, *10*, 1-9.

[8] a) G. Monreal Santiago, K. Liu, W. R. Browne, S. Otto, *Nat. Chem.* **2020**, *12*, 603-607; b) Z. Dadon, M. Samiappan, N. Wagner, G. Ashkenasy, *Chem. Commun.* **2012**, *48*, 1419-1421.

[9] a) A. R. K. Dinesh Gupta, *Can. J. Chem.* **1980**, *58*, 1350-1354; b) J. Li, J. M. A. Carnall, M. C. A. Stuart, S. Otto, *Angew. Chem. Int. Edit.* **2011**, *50*, 8384-8386.

[10] a) X. Du, J. Li, A. Welle, L. Li, W. Feng, P. A. Levkin, *Adv. Mater.* **2015**, *27*, 4997-5001; b) F. Klepel, B. J. Ravoo, *Org. Biomol. Chem.* **2017**, *15*, 3840-3842; c) L. Li, W. Feng, A. Welle, P. A. Levkin, *Angew. Chem. Int. Edit.* **2016**, *128*, 13969-13973.

[11] a) D. H. Lee, J. R. Granja, J. A. Martinez, K. Severin, M. R. Ghadiri, *Nature* **1996**, *382*, 525-528; b) M. Amit, S. Yuran, E. Gazit, M. Reches, N. Ashkenasy, *Adv. Mater.* **2018**, *30*, 1707083.

[12] R. Issac, J. Chmielewski, *J. Am. Chem. Soc.* **2002**, *124*, 6808-6809.

[13] a) A. Tököli, B. Mag, É. Bartus, E. Wéber, G. Szakonyi, M. A. Simon, Á. Czibula, É. Monostori, L. Nyitray, T. A. Martinek, *Chem. Sci.* **2020**, *11*, 10390-10398; b) B. F. Fisher, S. H. Hong, S. H. Gellman, *J. Am. Chem. Soc.* **2017**, *139*, 13292-13295.

[14] T. A. Martinek, I. M. Mándity, L. Fülöp, G. K. Tóth, E. Vass, M. Hollósi, E. Forró, F. Fülöp, *J. Am. Chem. Soc.* **2006**, *128*, 13539-13544.

[15] a) D. H. Appella, L. A. Christianson, D. A. Klein, D. R. Powell, X. Huang, J. J. Barchi, S. H. Gellman, *Nature* **1997**, *387*, 381-384; b) A. Hetényi, I. M. Mándity, T. A. Martinek, G. K. Tóth, F. Fülöp, *J Am Chem Soc* **2005**, *127*, 547-553.

[16] K. S. Iyer, W. A. Klee, *J. Biol. Chem.* **1973**, *248*, 707-710.

[17] H. R. Kilgore, R. T. Raines, *J. Phys. Chem. B* **2020**, *124*, 3931-3935.

[18] É. Bartus, Z. Hegedüs, E. Wéber, B. Csipak, G. Szakonyi, T. A. Martinek, *ChemistryOpen* **2017**, *6*, 236-241.

[19] a) A. Sorrenti, J. Leira-Iglesias, A. J. Markvoort, T. F. A. de Greef, T. M. Hermans, *Chem Soc Rev* **2017**, *46*, 5476-5490; b) D. Kondepudi, I. Prigogine, *Modern thermodynamics: from heat engines to dissipative structures*, John Wiley & Sons, **2014**.

[20] a) J. Boekhoven, A. M. Brizard, K. N. Kowlgi, G. J. Koper, R. Eelkema, J. H. van Esch, *Angew Chem Int Edit* **2010**, *49*, 4825-4828; b) S. Maiti, I. Fortunati, C. Ferrante, P. Scrimin, L. J. Prins, *Nat Chem* **2016**, *8*, 725-731.

[21] a) P. G. Higgs, *J. Mol. Evol.* **2017**, *84*, 225-235; b) G. von Kiedrowski, in *Bioorganic chemistry frontiers*, Springer, **1993**, pp. 113-146.

[22] a) V. Diemer, N. Ollivier, B. Leclercq, H. Drobecq, J. Vicogne, V. Agouridas, O. Melnyk, *Nat. Commun.* **2020**, *11*, 2558; b) A. Canal-Martín, R. Pérez-Fernández, *Nat. Commun.* **2021**, *12*, 163.

[23] a) S. Maiti, I. Fortunati, C. Ferrante, P. Scrimin, L. J. Prins, *Nat. Chem.* **2016**, *8*, 725-731; b) J. L. England, *Nat. Nanotechnol.* **2015**, *10*, 919-923.

[24] R. D. Astumian, *Nat Commun* **2019**, *10*, 1-14.

[25] a) A. D. Corbett, J. D. Cheeseman, R. J. Kazlauskas, J. L. Gleason, *Angew. Chem. Int. Edit.* **2004**, *43*, 2432-2436; b) Q. Ji, R. C. Lirag, O. S. Miljanic, *Chem Soc Rev* **2014**, *43*, 1873-1884.

[26] G. Ashkenasy, T. M. Hermans, S. Otto, A. F. Taylor, *Chem Soc Rev* **2017**, *46*, 2543-2554.

[27] a) L. Liu, Y. Zou, A. Bhattacharya, D. Zhang, S. Q. Lang, K. Houk, N. K. Devaraj, *Nat Chem* **2020**, *12*, 1029-1034; b) C. Pezzato, L. J. Prins, *Nat Commun* **2015**, *6*, 7790; c) J. Boekhoven, W. E. Hendriksen, G. J. Koper, R. Eelkema, J. H. van Esch, *Science* **2015**, *349*, 1075-1079.

[28] a) P. Remon, D. Gonzalez, S. Li, N. Basilio, J. Andreasson, U. Pischel, *Chem Commun* **2019**, *55*, 4335-4338; b) P. K. Kundu, D. Samanta, R. Leizrowice, B. Margulis, H. Zhao, M. Börner, T. Udayabhaskararao, D. Manna, R. Klajn, *Nat Chem* **2015**, *7*, 646-652.

[29] a) P. Canavelli, S. Islam, M. W. Powner, *Nature* **2019**, *571*, 546-549; b) C. S. Foden, S. Islam, C. Fernández-García, L. Maugeri, T. D. Sheppard, M. W. Powner, *Science* **2020**, *370*, 865-869.

[30] E. Guseva, R. N. Zuckermann, K. A. Dill, *Proc. Natl. Acad. Sci. USA* **2017**, *114*, E7460.

Supporting Information

Light-fuelled primitive replication and selection in evolvable biomimetic chemical networks

Éva Bartus[a,b], Attila Tököli[a], Beáta Mag[a], Áron Bajcsi[a], Gábor Kecskeméti[a], Edit Wéber[a], Zoltán Kele[a], Gabriel Fenteany[a,c], Tamás A. Martinek[a,b]*

[a] É. Bartus, A. Tököli, B. Mag, Á. Bajcsi, G. Kecskeméti, E. Wéber, Z. Kele, T. A. Martinek
Department of Medical Chemistry
University of Szeged
Dóm tér 8, H-6720 Szeged, Hungary
E-mail: martinek.tamas@med.u-szeged.hu

[b] É. Bartus, T. A. Martinek
MTA-SZTE Biomimetic Systems Research Group
University of Szeged
Dóm tér 8, H-6720 Szeged, Hungary

[c] G. Fenteany
Institute of Genetics
Biological Research Centre
Temesvári krt. 62, H-6726 Szeged, Hungary

Table of Contents

Experimental Procedures

UV-fuelled disulfide exchange reaction

Twelve different monomers were dissolved in 20 mM HEPES, 150 mM NaCl, 2 mM $CaCl_2$ (pH = 7.0), with each monomer at a final concentration of 10 μM. The reaction mixture was transferred into quartz cuvettes having a PTFE stopper and kept under an argon atmosphere during the experiment. Solutions were stirred at 150 RPM and kept at a constant temperature of 303 ± 1 K with an air-cooling system (modified Jasco Jetstream 2 Plus Column Thermostat). The temperature was monitored with a laser gun thermometer. Continuous illumination of the samples was carried out with a UVL-28 EL Series UV lamp (Analytic Jena US, Upland, CA). The distance dependence of the power density and the emission spectrum of the lamp were determined prior to the experiments (Figure S6), and the irradiation intensity was controlled by the distance between the lamp and the sample (Figure S7). 200 μL samples were taken from the reaction mixture at each time point. Placing the sample in the dark froze the reaction; no relaxation to equilibrium occurred. To eliminate any slow non-photocatalytic disulfide exchange reaction in the mixture until the analysis, we added 100 μL of 10% TFA in water. The product distribution of the samples was analysed using HPLC/ESI-MS measurements.

LC-MS measurements and MS data analysis

LC-MS analysis was performed with a Dionex UltiMate 3000 HPLC system interfaced with an LTQ ion trap mass spectrometer (Thermo Electron Corp., San Jose, CA, USA). Samples were injected onto an Aeris™ Widepore XB-C18 (250 × 4.6 mm, particle size: 3.6 μm, pore size 100Å) analytical HPLC column using gradient elution 5-80% solution B for 25 min at 0.7 mL min^{-1} flow rate. Eluent composition was 0.1% formic acid in distilled water (Solution A) and 0.1% formic acid in acetonitrile (Solution B). The MS instrument was operated in the positive-ion mode using the equipped HESI-II source with the following parameters: capillary temperature: 350°C; spray voltage: 3.0 kV; source heater temperature: 250°C; sheath gas flow: 30 mL min^{-1}; aux gas flow: 10 mL min^{-1}. Mass spectra were acquired in full-scan mode from 200 to 2000 *m/z*. Thermo Xcalibur 2.2 software was used for peak identification and integration. 96% of the foldameric building blocks could be resolved independently by HPLC-MS/MS measurements based on molecular weight, MS fragmentation pattern and retention time depending on the relative hydrophobicity of the side chains. Those components which could not be resolved independently were integrated and averaged. A representative raw file for the library was utilised to create a processing method, where each sample component was associated with a chromatographic peak based on the previously identified mass (*m/z*) and retention time (Table S1). Using the ICIS peak detection algorithm, the general detection and integration criteria were: smoothing points: 5; baseline window: 60; area noise factor: 5; peak noise factor: 10. All raw data files were reprocessed with these processing setups together and analysed. Errors in peak identification during the automatic processing were corrected manually.

Synthesis and purification of the foldameric sequences

Foldameric sequences having L-Gly-L-Gly-L-Cys C-terminal segments were synthesised manually by standard solid-phase peptide synthesis with Fmoc/tBu chemistry. Rink Amide AM resin was used as solid support (capacity: 0.71 mmol/g) and HATU (1-[bis(dimethylamino)methylene]-1*H*-1,2,3-triazolo[4,5-b]pyridinium 3-oxid hexafluorophosphate) as coupling reagent in the presence of DIEA (*N,N*-diisopropylethylamine). Amino acids and coupling reagents were used in excess of 3 equivalents and shaking was applied at room temperature for 3 h. Deprotection was carried out in a DMF (*N,N*-dimethylformamide) solution containing 2% DBU (1,8-diazabicycloundec-7-ene) and 2% piperidine. Cleavage was performed with TFA/H_2O/DTT (DL-dithiothreitol)/TIS (triisopropylsilane) (90:5:2.5:2.5), which was followed by precipitation in ice-cold diethyl ether. The resin was washed with acetic acid and water, filtered, then lyophilised. Peptides were purified by RP-HPLC on a C18 column (Phenomenex Luna C18, 250 x 10.00 mm, particle size: 10 μm, pore size: 100 Å). The HPLC eluents were 0.1% TFA in water (Eluent A), and 0.1% TFA/ 80% ACN (acetonitrile) in water (Eluent B). Different gradient elution was used according to the hydrophobicity of the peptides. Purity was confirmed by analytical RP-HPLC and ESI-MS measurements.

Synthesis and purification of the glutathione protected monomers

Glutathione-protected monomers were synthesised by oxidative coupling of thiols in the solution phase. Each purified foldamer was dissolved in 20% DMSO (dimethyl sulfoxide) in water separately to 1 mM concentration in the presence of 20× excess of GSH (reduced glutathione) and stirred overnight at room temperature exposed to atmospheric oxygen. The completeness of the oxidation reaction was monitored by HPLC-MS, and the reaction mixture was injected directly onto a semi-preparative HPLC column (Phenomenex Luna C18, 250 × 10.00 mm; particle size: 10 μm; pore size: 100 Å) and purified. Under this reaction condition the amount of the homodimeric foldamer was negligible and could be completely separated from the foldamer-glutathione adduct.

LC-MS analysis of the purified glutathione protected monomers

UHPLC-MS/MS measurements were used to characterize the pure peptides by using an ACQUITY I-Class UPLC™ liquid chromatography system (Waters, Manchester, UK) coupled with a Q Exactive™ Plus Hybrid Quadrupole-Orbitrap Mass Spectrometer (Thermo Fisher Scientific, San Jose, CA, USA). Chromatographic separation was carried out at 25 °C using 0.1% formic acid in water as solvent A and ACN containing 0.1% formic acid as solvent B. The following multistep gradient was used: 5-50% over 20 minutes then 50-80% over 5 minutes and finally 80% solvent B for additional 5 minutes at 0.7 mL min^{-1} flow rate. Samples where incubated at 5°C until the measurement and 15 µL of the sample was injected into the UHPLC–MS/MS system. The MS instrument was operated in the positive-ion mode using the equipped HESI-II source with the following parameters: capillary temperature: 256°C; spray voltage: 3.5 kV; aux gas heater temperature: 412°C; sheath gas flow: 47.5 mL min^{-1}; aux gas flow: 11 mL min^{-1}; and S-lens RF level, 50.0 (source auto-defaults). Full scan was conducted with a mass range of 150–2000 *m/z* with resolution of 70,000. The ACG (automatic gain control) setting was defined as 3×10^6 charges, and the maximum injection time was set to 100 ms. Data dependent MS/MS was acquired in a mass range of 200-2000 *m/z* with resolution of 17,500. AGC setting was defined as 5×10^5 charges, and the maximum injection time was set to 150 ms.

Preliminary experiments for testing disulfide rearrangement in a foldamer library

Two setups for the starting systems were used for testing. First, four different glutathione protected monomers, **WF-G, RW-G, LW-G** and **TW-G** were dissolved in 20 mM HEPES buffer with 150 mM NaCl and 2 mM $CaCl_2$ (pH=7.0) each one in 10 µM concentration. Second, the 10-membered dimeric library was prepared by slow oxidation of the thiol forms of the foldamers, **WF-SH, RW-SH, LW-SH** and **TW-SH**, which formed the statistical concentration distribution. The components were transferred into the previously defined buffer so that each heterodimer had a concentration of 10 µM. An excess of oxidized glutathione (500 µM) was added to this latter mixture. The reaction mixtures were transferred separately into quartz cuvettes having PTFE stopper and kept under argon atmosphere during the experiment. Solutions were stirred at 150 RPM and kept at constant temperature of 303±1 K *via* air cooling system. Continuous irradiation of the samples was carried out by UVL-28 EL Series UV Lamp at 365 nm (Analytic Jena US, Upland, CA). Product distribution was monitored with HPLC-MS. To directly test the effect of UV in the disulfide rearrangement, a control experiment was performed from the mixtures and kept under the same condition but without UV-irradiation.

Generating statistical dimer distribution and calibration of the MS-AUC-to-concentration conversion

Statistical product distribution for the dimers were generated in a chaotropic solvent mixture of 20% DMSO:80% water. Glutathione-protected monomers were dissolved (each one at 10 µM final concentration) and the library was completely reduced with 2 molar equivalents of TCEP (tris(2-carboxyethyl)phosphine). Subsequently, the sample was continuously stirred for 48 h exposed to atmospheric oxygen.

To confirm that oxidation in the chaotropic solvent (DMSO:water) results in statistical product distribution, a subset of monomers was analysed for which self-association tendency is significantly different (Extended Data Fig. 1) (**WF-G**, **LW-G**, **RW-G** and **TW-G**). The oxidised mixture was analysed using HPLC-UV with the detection wavelength of 210 nm, where the integrated intensity is directly proportional to the peptide concentration. For this system, the oxidation products could be quantitatively analysed in HPLC-UV without problem. As expected, the reaction yielded four homodimers and six heterodimers with statistical concentration distribution (Figure S8).

Next, we performed the same experiment starting from the 12-membered monomer library. Completeness of the oxidation after the TCEP treatment was confirmed, and the final product distribution was quantitatively analysed with HPLC-MS. Due to the large number of components, UV detection could not separate the products. Based on the model experiment, the statistical concentration of each dimer was predicted and then calculated. After the quantitative evaluation of the HPLC-MS chromatograms, the MS-AUC/concentration ratios were calculated for each component (Table S4).

Generating equilibrium dimer distribution through thiolate-mediated exchange

The twelve different thiol-functionalized foldameric building blocks (**IF-SH, KW-SH, LW-SH, QW-SH, RW-SH, RF-SH, SW-SH, TW-SH, VW-SH, WF-SH, WW-SH** and **YF-SH**) were dissolved at a concentration of 10 µM in a redox buffer (pH 8.0, 20 mM HEPES, 150 mM NaCl, 1 mM CaCl2, 3 mM NaN3, 500 µM GSH and 125 µM GSSG). Reaction mixture was shaken at 250 rpm, 37°C for three days in a properly closed vial. Samples (100 µL) were taken from the mixture every 24 h, quenched with 10% TFA in water (50 µL) and analysed with HPLC-MS[1]. Product distribution was obtained via quantitative evaluation of the HPLC-MS chromatograms and conversion of AUC-to-concentration was carried out as described above (Figure S3-S4).

Calculation of the light intensity-dependent amplification factor

Light intensity-dependent amplification factors (AF) were calculated for each dimer to determine the sensitivity to the energy influx. The following formula (eq. (S12)) was used:

$$AF_{i(C),int} = \frac{AUC_{i(C),100\%}}{AUC_{i(C),50\%}} \quad \text{(S12)}$$

where $AUC_{i(C),100\%}$ is the area under the curve (AUC) of compound *i* measured at 100% light intensity (5.10 mW cm^{-2}) and $AUC_{i(C),50\%}$ is the AUC of the same compound measured at 50% light intensity (2.55 mW cm^{-2}). Errors of AF_i (σ_{AF}) were calculated from three parallel measurements with the following general formula (neglecting the correlation between the variables):

$$\sigma_{AFi} = AF_i \sqrt{\left(\frac{\sigma_{AUC1}}{AUC_1}\right)^2 + \left(\frac{\sigma_{AUC2}}{AUC_2}\right)^2} \quad \text{(S13)}$$

where $AUC_1 \pm \sigma_{AUC1}$ and $AUC_2 \pm \sigma_{AUC2}$ are the measured variables with uncertainties when AF_i is calculated by AUC_1/AUC_2.

Calculation of the concentration amplifications for the dimers upon seeding

Concentration amplifications (CA) were calculated for each dimer to evaluate the catalytic effect of seeding dimer (**WF-S-YF**). The following formula (S14) was used for the calculation:

$$CA_{i,seeding} = \frac{AUC_{i,seeded}}{AUC_{i,control}} \quad \text{(S14)}$$

Where $AUC_{i,\ seeded}$ is the area under the curve (AUC) of compound i measured in the presence of the seeding compound and $AUC_{i,\ control}$ is the AUC of the same compound measured without the seeding compound.

Calculation of the side chain enrichment

Enrichment (E) of the proteinogenic side chains in the peripheral (1, 1′) and the central (2, 2′) positions of the ten most amplified dimers was expressed as the frequency of a side chain relative to all side chains in the foldamer system by using the following formula (S15):

$$E_{schi} = \frac{N_{schi,Best}/10}{N_{schi,All}/78} \quad \text{(S15)}$$

Where E_{schi} is the enrichment of the side chain *i* in appropriate position, $N_{schi,Best}$ is the count of the side chain *i* among the top ten amplified dimers, $N_{schi,All}$ is the count of the side chain *i* in the complete system.

Supplementary Text

Equation (1): Rate of spontaneous dimer synthesis through diffusion-controlled radical substitution

In this mechanism, dimers (MSSM) are produced by the reaction of freely diffusing monomer radicals (MS·) with glutathione-protected monomers (MSSG) as shown in reaction [3a] (Figure 1b). Here, "MS" corresponds to a single foldameric sequence.

$$\text{MSSG} + \text{MS}^{\bullet} \longrightarrow \text{MSSM} + \text{GS}^{\bullet} \quad \text{[3a]}$$

The reaction rate for [3a] ($v_{s,ch}$) satisfies eq. (S1),

$$v_{s,ch} = k_{ch}[\text{MS}\cdot][\text{MSSG}] \quad \text{(S1)}$$

where k_{ch} is the rate constant for the radical substitution step. In radical chain reactions, [MS·] can be approximated with a quasi-steady state approach. At low conversions, MS· is produced preferentially by homolytic cleavage of the starting material MSSG. Therefore, the rate of formation is proportional to the light intensity ($k_I I$) and [MSSG]. The chain-termination steps consuming MS· involve collisions with MS· and GS·. Again, the large excess of MSSG at low conversions affords the approximation that reaction [1a] (Figure 1b) is dominant. Thus, there is a 12× molar excess for [GS·], that is, [GS·] ≈ 12[MS·]. Consequently, the chain-termination rate can be expressed as a second order function in [MS·] (eq. (S2)).

$$\frac{d[MS^{\cdot}]}{dt} = 0 = k_I I[\mathrm{MSSG}] - k_t[\mathrm{MS}^{\cdot}]^2 - k_t 12[\mathrm{MS}^{\cdot}]^2 \quad \text{(S2)}$$

$$[\mathrm{MS}^{\cdot}] = \sqrt{\frac{k_I I}{13k_t}[\mathrm{MSSG}]} \quad \text{(S3)}$$

Here, k_I is the rate constant of the light-induced homolytic cleavage, and k_t is the rate constant for the chain-termination reaction. Substituting eq. (S3) into eq. (S1) and collecting the concentration- and light intensity-independent terms into the constant s_{ch}, the rate is given by eq. (1).

$$v_{s,ch} = s_{ch}\sqrt{I}[\mathrm{MSSG}]^{1.5} \quad (1)$$

Equation (2): Rate of dimer breakdown through diffusion-controlled radical substitution

The decomposition of MSSM proceeds in this mechanism through the reaction between the freely diffusing glutathione radical ($GS^{\cdot}$) and MSSM (reaction [3b]).

$$\mathrm{MSSM} + \mathrm{GS}^{\bullet} \longrightarrow \mathrm{MSSG} + \mathrm{MS}^{\bullet} \quad \text{[3b]}$$

The rate equation can be expressed as follows (eq. (S4)).

$$v_b = k_b[\mathrm{GS}^{\cdot}][\mathrm{MSSM}] \quad \text{(S4)}$$

For $[GS^{\cdot}]$, we apply the quasi-steady state approximation again. The source of $[GS^{\cdot}]$ is the light-induced homolytic cleavage of MSSG and GSSG. The chain-termination steps consuming $GS^{\cdot}$ involve collisions with $GS^{\cdot}$ and $MS^{\cdot}$. Due to the 12× excess of $GS^{\cdot}$ over $MS^{\cdot}$ in the system studied, the latter reaction can be neglected. Thus, we obtain eq. (S5).

$$\frac{d[\mathrm{GS}^{\cdot}]}{dt} = 0 = k_I I([\mathrm{MSSG}] + 2[\mathrm{GSSG}]) - k_t[\mathrm{GS}^{\cdot}]^2 \quad \text{(S5)}$$

Due to the mass balance for the 'GS' moiety, the term [MSSG] + 2[GSSG] is constant and equals to the initial concentration of MSSG ($[MSSG]_0$), which yields eq. (S6).

$$[\mathrm{GS}^{\cdot}] = \sqrt{\frac{k_I I}{k_t}[\mathrm{MSSG}]_0} \quad \text{(S6)}$$

Thus, $[GS^{\cdot}]$ is proportional to the square root of the light intensity, and eq. (S6) can be substituted into (S4). Collecting the constant term into the overall rate constant of *b*, we obtain eq. (2).

$$v_b = b\sqrt{I}[\mathrm{MSSM}] \quad (2)$$

Equations (3) and (4): Rates of dimer synthesis through proximity-controlled mechanisms

This mechanism begins with the association preequilibrium producing the complex $(MSSG)_2$.

$$2\ \mathrm{MSSG} \rightleftharpoons (\mathrm{MSSG})_2 \quad [5]$$

$$[(\mathrm{MSSG})_2] = \frac{1}{K_{D,p}}[\mathrm{MSSG}]^2 \quad (S7)$$

$K_{D,p}$ stands for the dissociation constant. The rate-determining step is the photochemical cleavage of a monomer within the complex (reaction [6]). If the geometry of the complex is advantageous, the resulting high-energy radical can rapidly relax through the intracomplex radical substitution [7].

$$(\mathrm{MSSG})_2 \xrightarrow{+\,h\nu} \mathrm{MSSG\text{-}MS^{\bullet}} + \mathrm{GS^{\bullet}} \quad [6]$$

$$\mathrm{MSSG\text{-}MS^{\bullet}} \longrightarrow \mathrm{MSSM} + \mathrm{GS^{\bullet}} \quad [7]$$

The rate of formation for MSSG-MS· is proportional to the light intensity ($k_I I$) and [$(MSSG)_2$]. Using eq. (S7), the rate equation can be obtained (eq. (S8)).

$$v_{s,p1} = \frac{k_I I}{K_{D,p}}[\mathrm{MSSG}]^2 \quad (S8)$$

Substituting the constant term with the overall rate constant s_{p1} yields eq. (3).

$$v_{s,p1} = s_{p1} I [\mathrm{MSSG}]^2 \quad (3)$$

Literature results showed that recombination of two thiyl radicals is a possible photochemical exchange mechanism, when radical substitution is sterically hindered[2]. Therefore, the intracomplex version of this mechanism cannot be ruled out *a priori*. If the absorption of the two photons is consecutive, the reaction rate remains first order in light-intensity; that is, the functional form of the rate equation is the same as eq. (3). If coincident absorption of two photons produces the diradical intermediate $(MS\cdot)_2$ and MSSM is formed in a concerted manner (steps [8] and [9]), the probability of the interaction with two photons is proportional to the square of the light intensity.

$$(\mathrm{MSSG})_2 \xrightarrow{+\,2\,h\nu} (\mathrm{MS^{\bullet}})_2 + 2\ \mathrm{GS^{\bullet}} \quad [8]$$

$$(\mathrm{MS^{\bullet}})_2 \xrightarrow{-\,\Delta} \mathrm{MSSM} \quad [9]$$

The cross-section of the interaction is not decreased by the non-linear “two-photon absorption” effect, because disulfides in the complex are not coupled quantum mechanically. Moreover, the recombination of the diradical [9] does not involve any activation energy, leading to a very fast reaction. On this ground, we incorporated this mechanism into the model with the rate equation (4).

$$v_{s,p2} = s_{p2} I^2 [\mathrm{MSSG}]^2 \quad (4)$$

Equations (5) and (6): Rates of autocatalytic dimer synthesis

The autocatalytic mechanism starts with a binding preequilibrium between the dimers and the monomers ([10]). The dissociation constant ($K_{D,a}$) determines the concentration of the complex available for the further, rate determining step.

$$2\ \mathrm{MSSG} + \mathrm{MSSM} \rightleftharpoons \mathrm{MSSM\text{-}(MSSG)_2} \quad [10]$$

$$[\mathrm{MSSM\text{-}(MSSG)_2}] = \frac{1}{K_{D,a}}[\mathrm{MSSM}][\mathrm{MSSG}]^2 \quad (S9)$$

The calculation of the rates for the autocatalytic routes is closely analogous to the non-autocatalytic synthesis pathways described above. For the intracomplex radical-substitution pathway, the rate-determining step is the absorption of a photon, which leads to a linear light-intensity dependence of the reaction rate. Using (S9), eq. (6) is obtained.

$$v_{s,a1} = s_{a1} I [\mathrm{MSSM}][\mathrm{MSSG}]^2 \quad (6)$$

Coincident absorption and the concerted conversion to MSSM is also possible for the autocatalytic complex, which yields a rate equation quadratic in light intensity (eq (7)).

$$v_{s,a2} = s_{a2} I^2 [\mathrm{MSSM}][\mathrm{MSSG}]^2 \quad (7)$$

Dynamic model for the foldamer-based photochemical disulfide exchange system

The mathematical framework of chemical evolution[3] was invoked to analyse the experimentally determined energy-dependent dynamics of the dimer synthesis. The differential equation describing the time- and light intensity-dependent concentration of the dimers ([MSSM]) contained the following rate terms (eq. (S10)): non-autocatalytic (spontaneous) synthesis ($v_{s,p1}$ and $v_{s,p2}$), autocatalytic synthesis ($v_{s,a1}$ and $v_{s,a2}$) and break down (v_b).

$$\frac{d[\mathrm{MSSM}]}{dt} = v_{s,p1} + v_{s,p2} + v_{s,a1} + v_{s,a2} - v_b \quad (S10)$$

Fitting the dynamic model to the experimental time- and energy-dependent data arrays

Differential equation (S10) was numerically integrated using the Runge-Kutta (RK4) method to simulate the light intensity-dependent time evolution of a dimer. The synthesis rates are dependent on the actual monomer concentration, which was expressed with [MSSM] using the mass balance (S11).

$$[\mathrm{MSSG}] = [\mathrm{MSSG}]_0 - 2[\mathrm{MSSM}] \quad (S11)$$

The numeric integrations were carried out with the parameters of $[\mathrm{MSSM}]_0 = 0$, $[\mathrm{MSSG}]_0 = 2\times10^{-5}$ M and $\Delta t = 4.17\times10^{-2}$ h. The light intensities were set to the calibrated values. The rate constants s_{p1}, s_{p2}, s_{a1}, s_{a2} and b were determined by fitting (non-linear regression) the simulated curves against the time- and light intensity-dependent experimental data array.

Supplementary Figures

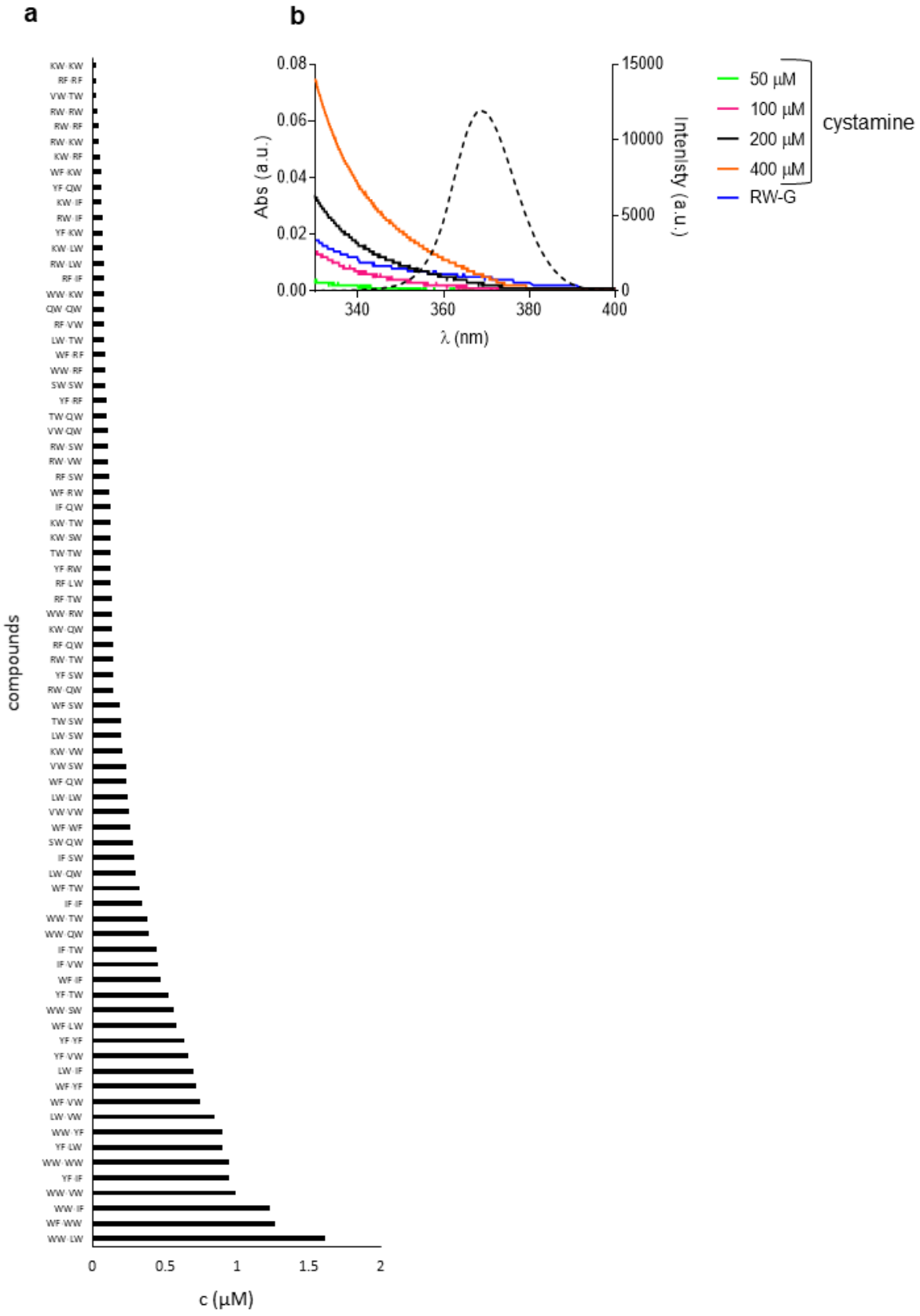

Figure S1. The equilibrium product distribution of foldameric dimers and UV spectra of the disulfide containing samples. a) Equilibrium product distribution was measured in an aqueous solution; for the experimental conditions, see Supplementary Methods. **b**) UV spectra of cystamine solutions in the range of 330-400 nm. UV spectrum of the representative monomer **RW-G** at the concentration of 120 μM. The dashed curve shows the emission spectrum of the UV lamp (UVL-28 EL Series UV Lamp) in the range of 330-400 nm.

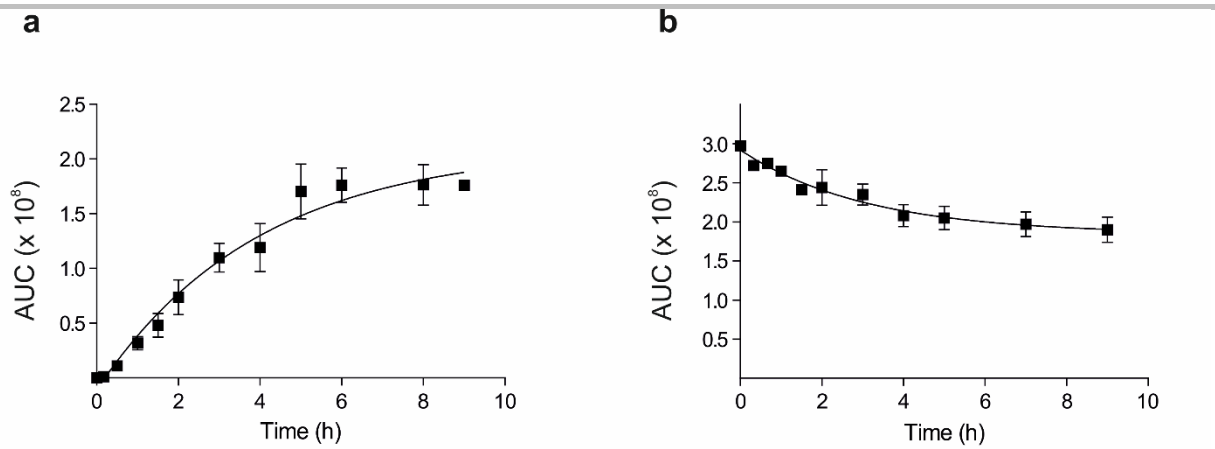

Figure S2. Representative concentration changes given for the monomer RW-G as a result of UVA irradiation (365 nm). (**a**) Decomposition of RW-containing dimers leads to the formation of the monomer **RW-G**. Undesired side products were not detectable during the measurement. (**b**) Concentration decay of the monomer **RW-G** due to dimer formation.

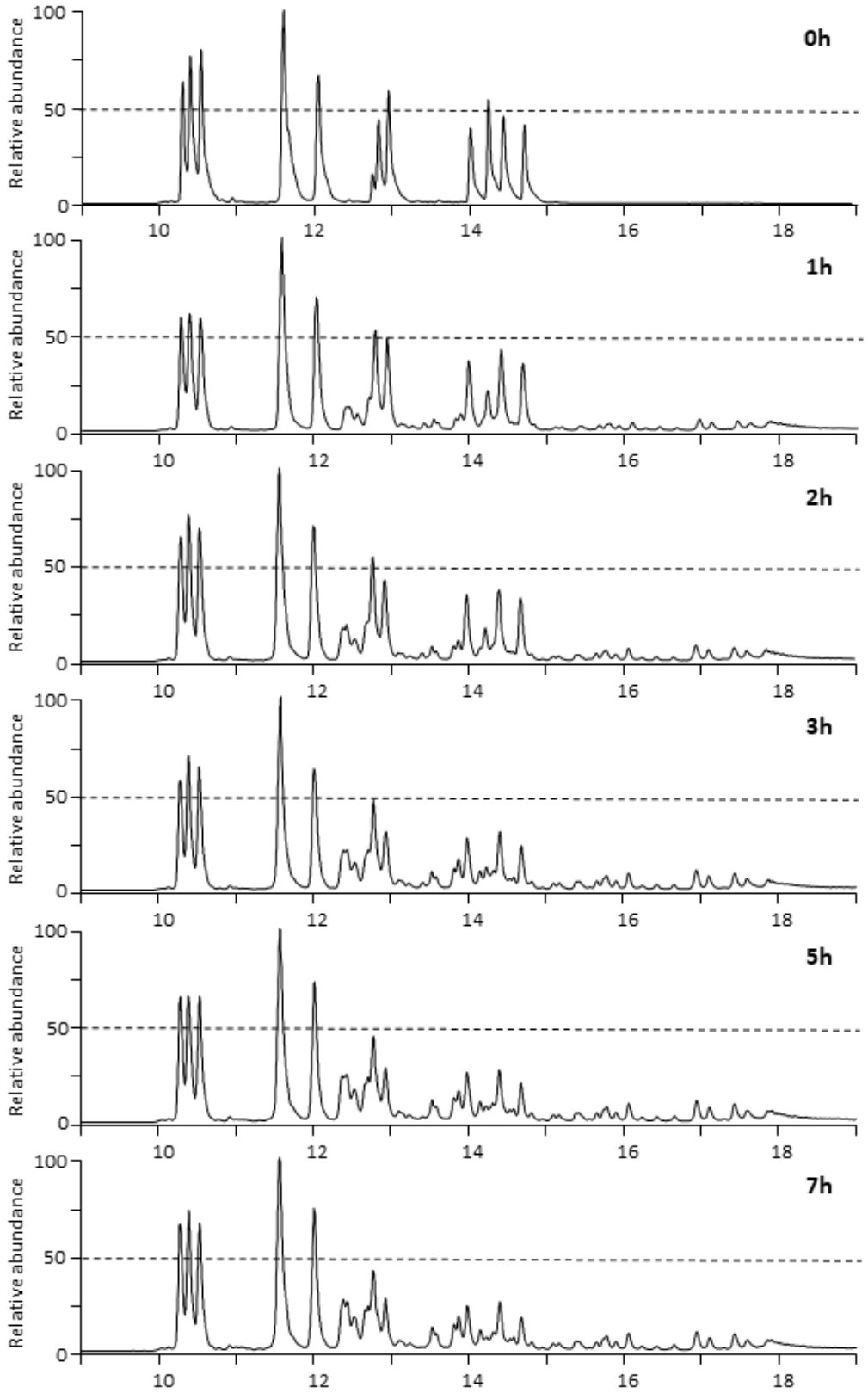

Figure S3. Representative total ion chromatograms of the foldameric mixture obtained at the power density of 5.10 mW cm^{-2}. Samples were analysed at the given time points. Conditions of the analysis: Column: Aeris Widepore XB-C18 (250 x 4.6 mm). Method: 5–80% B during 25 min, flow rate: 0.7 mL min^{-1}, where eluent A: 0.1% HCOOH in water, eluent B: 0.1% HCOOH in acetonitrile.

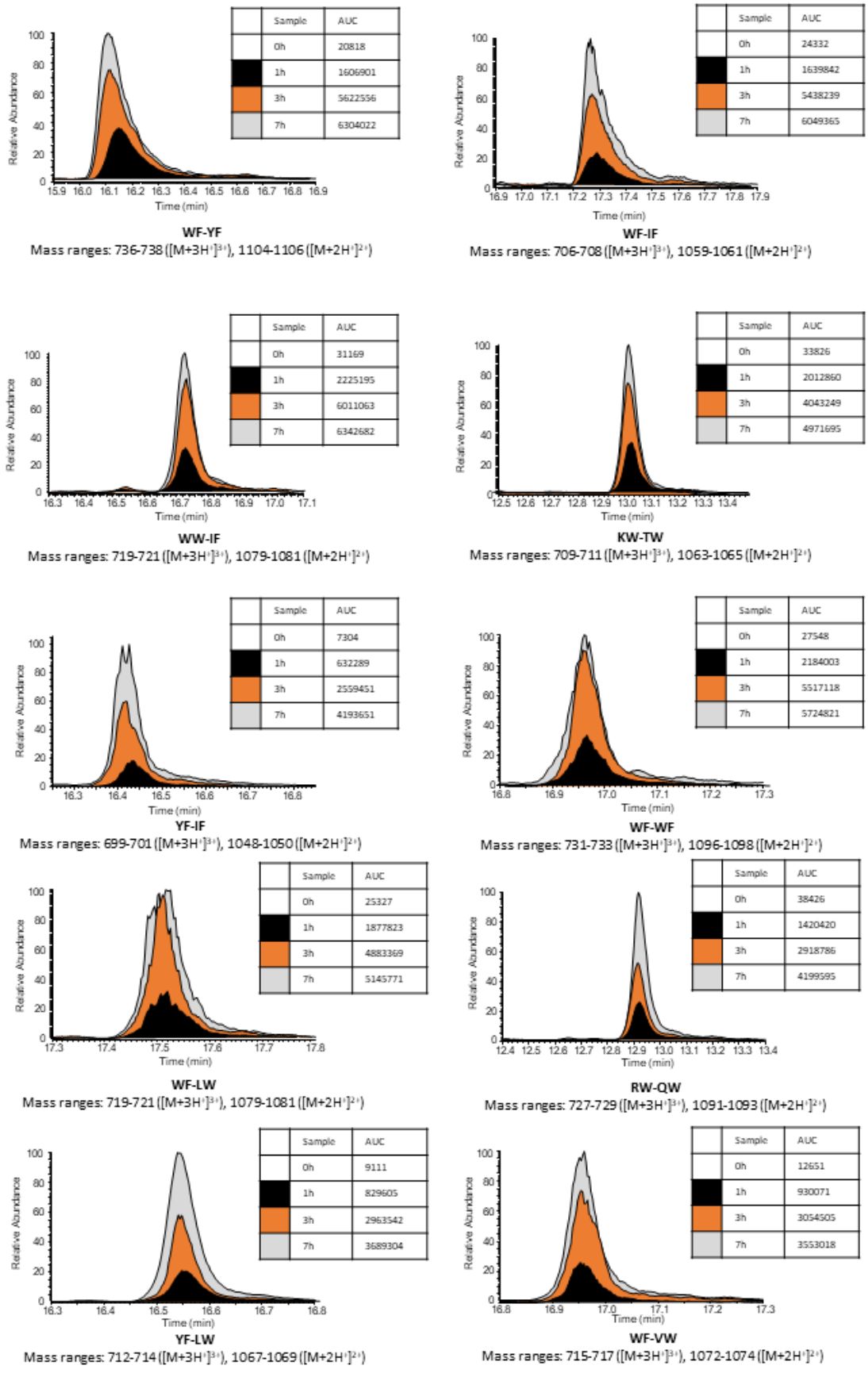

Figure S4. Extracted ion chromatograms of the given representatives obtained at power density of 5.10 mW cm^{-2}. Samples were measured at different time points (after 1, 3 and 7 h, black, orange and grey, respectively), intensity of the signal was observed at the given mass-to range values.

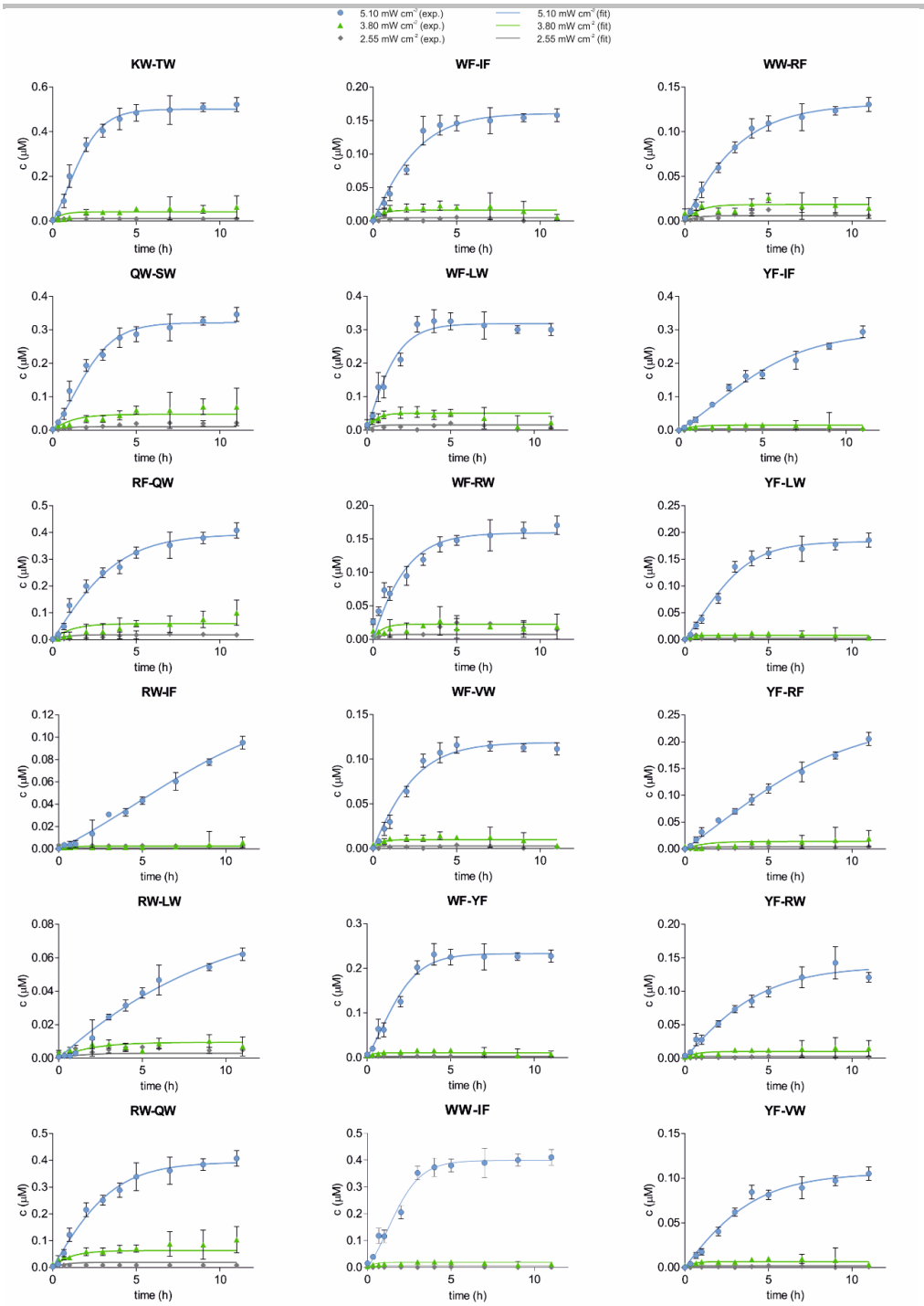

Figure S5. Fitting of the dynamic model to the light intensity and time-dependent data arrays measured for representative replicators. Data at different light intensities are represented as follows: 2.55 mW cm^{-2} (gray diamond), 3.80 mW cm^{-2} (green triangle) and 5.10 mW cm^{-2} (blue circle); fitted curves are depicted with matching color. Non-linear least-squares analysis was used for fitting. Experimental data were obtained from three parallel measurements on three different samples. See Supplementary Table 2 for fitted parameters.

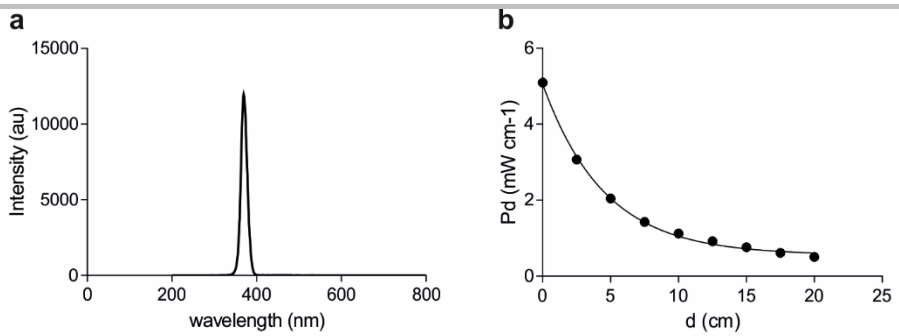

Figure S6. Calibration of the UV light source. (**a**) The emission spectrum of the UV light source (UVL-28 EL Series UV Lamp), with an emission maximum at 365 ± 5 nm and (**b**) dependence of the power density (Pd [mW cm^{-2}]) on the distance. The power density was measured with an S140C Integrating Sphere Photodiode Power Sensor (Thorlab Inc.). The wavelength range of the Si detector was 350–1100 nm, and the power range was 1 µW–500 mW (resolution: 1 nW)

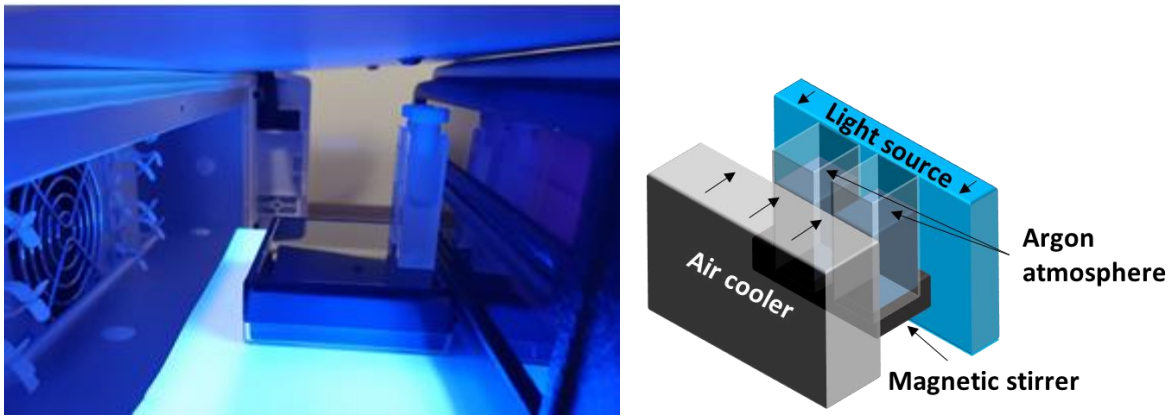

Figure S7. Photo and schematic representation of the experimental setup. The reaction mixtures were stirred at 150 RPM in quartz cuvettes having a PTFE stopper and kept under an argon atmosphere during the experiment. Constant temperature (303 ± 1 K) was maintained with *an* active air-cooling system (column thermostat). The temperature was monitored with a laser-gun thermometer. Continuous irradiation of the samples was carried out by UVL-28 EL Series UV lamp working at 365 nm (Analytic Jena US, Upland, CA), and the power density was varied by changing the distance between the light source and the samples.

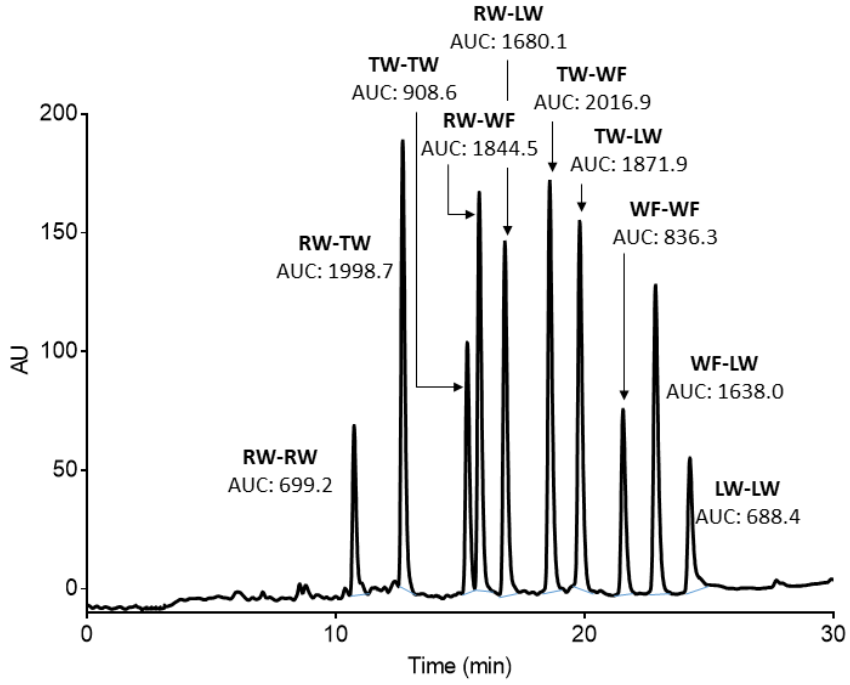

Figure S8. Product distribution obtained by slow oxidation in a chaotropic solvent. Oxidation of the glutathione-protected foldamers **WF-SG**, **LW-SG**, **RW-SG** and **TW-SG** resulted in a statistical product distribution despite their different tendencies to associate. Samples were analysed by HPLC-MS. Conditions of the analytical HPLC-MS measurement: column: Phenomenex Luna-C18 (250 x 4.6 mm); method: 5-80% B during 25 min, flow rate: 0.7 mL min^{-1}, where eluent A: 0.1% TFA in water, eluent B: 0.1% TFA in ACN: water = 8:1.

Supplementary Tables

Table S1. HPLC-MS characterisation of dimers and monomers in the system.

Compounds	Calculated molar mass (Da)	Retention time (min)[a]	Detected ions	
			$[M+2H^+]^{2+}$	$[M+3H^+]^{3+}$
IF-IF	2044.66	17.73	1022.95	682.29
IF-QW	2098.67	15.70	1049.79	700.47
IF-G	1327.62	14.49	664.84	443.54
IF-SW	2057.62	15.79	1029.89	686.75
IF-TW	2071.65	16.05	1036.42	691.59
IF-VW	2069.67	17.29	1035.41	690.82
KW-IF	2098.71	14.55	1049.79	700.00
KW-KW	2152.76	11.70	1077.40	718.48
KW-LW	2137.75	14.70	1069.44	713.56
KW-QW	2152.72	12.73	1076.93	718.90
KW-RF	2141.74	11.63	1071.41	714.82
KW-G	1381.69	10.42	691.85	461.56
KW-SW	2111.63	12.73	1056.87	705.04
KW-TW	2125.70	13.09	1063.35	709.34
KW-VW	2123.68	14.26	1063.34	708.73
LW-IF	2084.61	17.84	1042.52	695.41
LW-LW	2123.72	18.00	1062.03	708.28
LW-QW	2137.71	15.84	1069.41	713.77
LW-G	1366.68	14.76	684.35	456.56
LW-SW	2096.66	15.94	1048.90	700.19
LW-TW	2111.67	16.19	1056.01	704.69
LW-VW	2108.71	17.43	1054.60	703.40
QW-QW	2152.68	13.71	1077.12	718.79
QW-G	1381.65	11.60	691.83	461.55
RF-IF	2087.69	14.59	1044.38	697.05
RF-LW	2126.73	14.77	1063.94	709.58
RF-QW	2141.70	12.73	1071.37	715.15
RF-RF	2130.72	11.64	1066.67	710.97
RF-G	1370.68	10.31	686.35	457.89
RF-SW	2100.65	12.80	1050.89	701.43
RF-TW	2114.68	12.77	1057.93	706.26
RF-VW	2112.70	14.28	1056.99	705.03
RW-IF	2126.73	14.77	1064.57	709.87
RW-KW	2180.78	11.80	1091.33	728.04
RW-LW	2165.77	14.91	1083.50	722.76
RW-QW	2180.74	12.90	1090.87	728.20
RW-RF	2169.76	12.22	1085.36	724.15
RW-RW	2208.80	11.97	1104.90	737.47
RW-G	1409.69	10.56	705.85	470.90
RW-SW	2139.69	12.96	1070.38	714.39
RW-TW	2153.72	13.29	1077.46	718.90
RW-VW	2151.74	14.41	1076.35	718.45
SW-QW	2110.69	13.76	1056.41	704.63
SW-G	1340.63	11.60	671.32	447.88
SW-SW	2070.58	12.99	1035.86	690.84
TW-QW	2125.66	14.05	1063.25	709.33
TW-G	1354.64	12.06	678.33	452.55
TW-SW	2083.70	14.13	1042.93	695.92
TW-TW	2098.64	14.35	1049.99	700.56
VW-QW	2122.74	15.35	1063.00	708.79
VW-G	1352.66	14.05	677.34	451.89
VW-SW	2082.63	15.44	1042.40	695.14
VW-TW	2096.66	15.70	1049.37	699.79
VW-VW	2094.68	16.97	1048.03	698.88
WF-IF	2117.72	17.27	1059.49	706.71
WF-KW	2171.77	14.31	1086.48	724.64
WF-LW	2156.76	17.45	1078.90	719.64
WF-QW	2171.73	15.40	1086.93	724.91
WF-RF	2160.75	14.37	1081.34	721.03
WF-RW	2199.79	14.48	1100.43	734.51
WF-G	1400.66	14.29	701.34	467.89
WF-SW	2130.68	15.49	1065.95	711.30
WF-TW	2144.71	15.76	1073.20	715.93
WF-VW	2142.73	16.96	1071.97	715.50
WF-WF	2190.78	16.96	1095.93	731.76
WF-WW	2229.81	16.41	1115.44	744.44
WF-YF	2167.74	16.10	1084.52	723.76
WW-IF	2156.75	16.78	1078.99	719.84
WW-KW	2210.80	13.73	1105.93	738.15
WW-LW	2195.79	16.89	1098.46	732.71
WW-QW	2210.76	14.71	1105.98	737.87
WW-RF	2199.78	14.48	1100.43	734.51
WW-RW	2238.82	13.94	1120.36	747.47
WW-G	1439.67	12.86	720.84	480.89
WW-SW	2169.71	16.08	1086.53	725.38

WW-TW	2183.74	15.09	1092.55	728.13
WW-VW	2181.76	16.39	1091.41	728.06
WW-WW	2268.84	15.81	1135.45	757.47
WW-YF	2206.77	15.53	1103.89	736.72
YF-IF	2094.68	16.41	1047.94	699.11
YF-KW	2148.73	13.54	1075.00	717.42
YF-LW	2133.72	16.57	1067.86	712.64
YF-QW	2148.69	14.50	1074.93	717.02
YF-RF	2137.71	13.54	1069.47	713.51
YF-RW	2176.75	13.71	1088.93	726.82
YF-G	1377.66	12.98	689.83	460.22
YF-SW	2107.64	14.58	1054.34	703.55
YF-TW	2121.67	14.84	1061.45	707.98
YF-VW	2119.69	16.06	1060.47	707.47
YF-YF	2144.70	15.22	1073.30	715.89

[a]Analytical HPLC-MS measurement. Column: Aeris Widepore XB-C18 (250 x 4.6 mm). Method: 5–80% B during 25 min, flow rate: 0.7 mL min^{-1}, where eluent A: 0.1% HCOOH in water, eluent B: 0.1% HCOOH in acetonitrile.

Table S2. Fitted rate constants for representative dimers.

Compounds	s_{p1} M^{-1} (cm^2) W^{-1} s^{-1}	s_{p2} x 10^2 M^{-1} $(cm^2)^2$ W^{-2} s^{-1}	s_{a1} x 10^7 M^{-2} (cm^2) W^{-1} s^{-1}	s_{a2} x 10^{10} M^{-2} $(cm^2)^2$ W^{-2} s^{-1}	b x 10^{-2} $(cm^2)^{0.5}$ $W^{-0.5}$ s^{-1}	RMSD x 10^{-9} M s^{-1}
KW-TW	0.00	38.03	0.01	205.16	2.80	19.97
QW-SW	0.00	25.94	0.00	107.88	1.57	15.49
RF-QW	0.00	25.80	0.00	77.01	1.12	24.99
RW-IF	0.00	1.99	0.00	117.49	1.68	3.60
RW-LW	1.27	0.00	0.00	70.29	1.05	4.50
RW-QW	0.00	27.53	18.24	66.25	1.47	18.47
WF-IF	5.43	0.00	247.59	0.00	6.95	10.53
WF-LW	0.00	38.80	100.06	73.31	3.85	22.19
WF-RW	2.73	14.65	0.00	143.86	2.21	17.27
WF-VW	4.39	0.24	304.75	0.00	8.61	6.70
WF-YF	0.00	13.41	270.42	0.00	7.45	11.26
WW-IF	0.00	24.06	0.00	280.08	3.84	20.34
WW-RF	4.38	0.00	155.16	0.57	4.42	15.14
YF-IF	0.00	8.91	0.02	112.28	1.58	11.85
YF-LW	4.01	0.04	270.87	0.00	7.53	7.15
YF-RF	0.00	5.91	0.00	83.24	1.19	6.35
YF-RW	2.83	0.35	177.91	0.08	5.01	6.71
YF-VW	0.00	6.77	0.00	178.50	2.64	5.06

Mean standard deviation of the fitted parameters was estimated with jackknife resampling technique and it was found to be less than 3.4% in each case.
s_{p1}: rate constant of spontaneous synthesis by proximity-controlled radical substitution
s_{p2}: rate constant of spontaneous synthesis by proximity-controlled concerted metathesis
s_{a1}: rate constant of autocatalytic synthesis by proximity-controlled radical substitution
s_{a2}: rate constant of autocatalytic synthesis by proximity-controlled concerted metathesis
b: rate constant of dimers break down via diffusion-controlled radical substitution

Table S3. Characterisation of the glutathione-protected monomers.

Compounds	Exact mass (Da)	Detected ions		Retention time (min)[a]	Retention time (min)[b]
		$[M+1H^+]^{1+}$	$[M+2H^+]^{2+}$		
IF-G	1327.62	1328.67	664.84	20.81	14.49
KW-G	1381.69	1382.69	691.85	16.58	10.42
LW-G	1366.68	1367.68	684.35	21.79	14.76
QW-G	1381.65	1382.65	691.83	17.48	11.60
RF-G	1370.68	1371.69	686.35	16.62	10.31
RW-G	1409.69	1410.7	705.85	18.03	10.56
SW-G	1340.63	1341.63	671.32	17.23	11.60
TW-G	1354.64	1355.65	678.33	19.15	12.06
VW-G	1352.66	1353.67	677.34	20.11	14.05
WF-G	1400.66	1401.67	701.34	21.37	14.29
WW-G	1439.67	1440.68	720.84	17.23	12.86
YF-G	1377.66	1378.65	689.83	18.94	12.98

[a]Analytical HPLC-UV measurement. Column: Phenomenex Luna C18 (250 x 4.6 mm). Method: 5–80% B during 25 min, flow rate: 1.2 mL min^{-1}, where eluent A: 0.1% TFA in water, eluent B: 0.1% TFA and 80% ACN in water.
[b]Analytical HPLC-MS measurement. Column: Aeris Widepore XB-C18 (250 x 4.6 mm). Method: 5–80% B during 25 min, flow rate: 0.7 mL min^{-1}, where eluent A: 0.1% HCOOH in water, eluent B: 0.1% HCOOH in ACN.

Table S4. Calibration of the MS Area Under Curve (AUC) to concentration conversion for each component of the system.

Compounds	calculated concentration (μM)[a]	mean AUC	SD	Conversion factor: AUC/μM
IF-IF	0.2083	6738896	167227	**32346754**
IF-QW	0.4167	14321621	1021416	**34371864**
IF-G	5	233796364	12121312	**46759273**
IF-SW	0.4167	10250563	267887	**24601332**
IF-TW	0.4167	9781464	99474	**23475495**
IF-VW	0.4167	14658581	333948	**35180567**

KW-IF	0.4167	6984610	192959	**16763051**
KW-KW	0.2083	4688541	196654	**22505032**
KW-LW	0.4167	10931447	352192	**26235452**
KW-QW	0.4167	9592254	191099	**23021391**
KW-RF	0.4167	6041711	280144	**14500094**
KW-G	5	93498264	8075947	**18699653**
KW-SW	0.4167	10307687	34078	**24738429**
KW-TW	0.4167	11140758	215090	**26737798**
KW-VW	0.4167	11219383	61459	**26926498**
LW-IF	0.4167	13317251	59335	**31961377**
LW-LW	0.2083	5459491	232775	**26205601**
LW-QW	0.4167	7510246	171240	**18024575**
LW-G	5	71564374	1943793	**14312875**
LW-SW	0.4167	7846422	820359	**18831398**
LW-TW	0.4167	7877221	1158047	**18905315**
LW-VW	0.4167	11755384	350708	**28212900**
QW-QW	0.2083	2505601	113767	**12026904**
QW-G	5	154788096	3212397	**30957619**
RF-IF	0.4167	9685531	98651	**23245255**
RF-LW	0.4167	9423472	313860	**22616315**
RF-QW	0.4167	5395324	470128	**12948767**
RF-RF	0.2083	2600196	66430	**12480959**
RF-G	5	76355793	557309	**15271159**
RF-SW	0.4167	8404764	40877	**20171417**
RF-TW	0.4167	6458569	88664	**15500554**
RF-VW	0.4167	9015525	232567	**21637242**
RW-IF	0.4167	9139403	235650	**21934550**
RW-KW	0.4167	7268733	135533	**17444946**
RW-LW	0.4167	9690533	135870	**23257261**
RW-QW	0.4167	8128642	168034	**19508725**
RW-RF	0.4167	4839118	14804	**11613873**
RW-RW	0.2083	2840665	146521	**13635212**
RW-G	5	81307536	3537250	**16261507**
RW-SW	0.4167	9262117	211359	**22229063**
RW-TW	0.4167	5594796	220034	**13427499**
RW-VW	0.4167	10268484	436026	**24644341**
SW-QW	0.4167	7741284	52795	**18579067**
SW-G	5	214373675	971923	**42874735**
SW-SW	0.2083	4460048	9425	**21408267**
TW-QW	0.4167	6258758	7940	**15021007**
TW-G	5	205650252	4735772	**41130050**
TW-SW	0.4167	7866053	65835	**18878512**
TW-TW	0.2083	6984610	192959	**33526183**
VW-QW	0.4167	8395542	149336	**20149285**
VW-G	5	218439667	209807	**43687933**
VW-SW	0.4167	9549648	30622	**22919137**
VW-TW	0.4167	14321621	1021416	**34371864**
VW-VW	0.2083	6719439	16227	**32253357**
WF-IF	0.4167	16802806	261057	**40326702**
WF-KW	0.4167	12948964	294491	**31077488**
WF-LW	0.4167	14057330	138666	**33737565**
WF-QW	0.4167	9308290	140062	**22339878**
WF-RF	0.4167	9750493	108676	**23401163**
WF-RW	0.4167	5231109	21871	**12554652**
WF-G	5	229629674	1234010	**45925935**
WF-SW	0.4167	10201405	81613	**24483352**
WF-TW	0.4167	10261229	335150	**24626930**
WF-VW	0.4167	12943413	2777026	**31064167**
WF-WF	0.2083	9182636	141237	**44076722**
WF-WW	0.4167	7037382	357237	**16889704**
WF-YF	0.4167	11977596	184803	**28746208**
WW-IF	0.4167	6697741	203025	**16074566**
WW-KW	0.4167	7218262	137235	**17323816**
WW-LW	0.4167	6808518	206582	**16340430**
WW-QW	0.4167	4956501	97189	**11895592**
WW-RF	0.4167	5597430	97043	**13433822**
WW-RW	0.4167	5744039	55944	**13785683**
WW-G	5	154424106	809265	**30884821**
WW-SW	0.4167	7736738	259061	**18568158**
WW-TW	0.4167	6666086	237986	**15998593**
WW-VW	0.4167	6666086	237986	**15998593**
WW-WW	0.2083	2408501	253201	**11560822**
WW-YF	0.4167	4863880	87381	**11673302**
YF-IF	0.4167	8352642	1717484	**20046325**
YF-KW	0.4167	8037313	69720	**19289535**
YF-LW	0.4167	9072627	56896	**21774286**
YF-QW	0.4167	6032798	175591	**14478703**
YF-RF	0.4167	6941704	43753	**16660077**
YF-RW	0.4167	7672105	108675	**18413037**

YF-G	5	177069749	1736459	**35413950**
YF-SW	0.4167	6309200	101256	**15142069**
YF-TW	0.4167	6577118	44472	**15785071**
YF-VW	0.4167	10338711	140452	**24812887**
YF-YF	0.2083	2466209	13733	**11837825**

[a]Calculated from the statistical product distribution

Table S5. Concentration amplifications (CA) for the MSSM dimers upon seeding with WF-S-YF at 40 min..

compound #	compound	$CA_{i,\ 40\ min}$	$\sigma\ (CA_{i,\ 40\ min})$
1	**WF-IF**	3.97	0.26
2	**WF-VW**	3.96	0.09
3	**WF-YF**	3.73	0.12
4	**LW-VW**	3.65	0.06
5	**YF-IF**	3.48	0.20
6	**WW-YF**	3.42	0.06
7	**IF-IF**	3.30	0.01
8	**WF-WF**	2.98	0.10
9	**IF-VW**	2.96	0.08
10	**YF-LW**	2.91	0.08
11	**YF-VW**	2.89	0.05
12	**LW-LW**	2.88	0.22
13	**YF-YF**	2.82	0.03
14	**WF-WW**	2.81	0.16
15	**LW-IF**	2.78	0.29
16	**WF-RF**	2.74	0.06
17	**WW-LW**	2.67	0.13
18	**WW-VW**	2.61	0.09
19	**WW-WW**	2.60	0.12
20	**LW-SW**	2.58	0.13
21	**WW-IF**	2.53	0.04
22	**WF-LW**	2.41	0.13
23	**WW-QW**	2.37	0.02
24	**WW-TW**	2.35	0.01
25	**IF-TW**	2.32	0.01
26	**VW-VW**	2.32	0.02
27	**YF-SW**	2.30	0.08
28	**WF-QW**	2.27	0.12
29	**LW-TW**	2.26	0.14
30	**VW-SW**	2.26	0.31
31	**WW-SW**	2.25	0.00
32	**LW-QW**	2.20	0.20
33	**WF-TW**	2.18	0.06
34	**RW-LW**	2.16	0.43
35	**WW-RW**	2.13	0.30
36	**IF-SW**	2.10	0.09
37	**IF-QW**	2.06	0.07
38	**WF-SW**	2.02	0.37
39	**VW-QW**	1.97	0.02
40	**VW-TW**	1.90	0.09
41	**RF-TW**	1.89	0.09
42	**RW-RW**	1.87	0.35
43	**YF-QW**	1.82	0.06
44	**RF-QW**	1.80	0.09
45	**SW-QW**	1.75	0.02
46	**KW-LW**	1.74	0.01
47	**RW-SW**	1.72	0.04
48	**SW-SW**	1.72	0.09
49	**YF-RW**	1.72	0.07
50	**YF-RF**	1.70	0.06
51	**YF-TW**	1.68	0.00
52	**KW-QW**	1.67	0.10
53	**QW-QW**	1.67	0.14
54	**KW-KW**	1.63	0.21
55	**RW-QW**	1.63	0.05
56	**KW-IF**	1.62	0.06
57	**RF-RF**	1.61	0.23
58	**RF-IF**	1.61	0.11
59	**WF-RW**	1.60	0.13
60	**WW-RF**	1.60	0.04
61	**RF-LW**	1.60	0.15
62	**RW-IF**	1.60	0.15
63	**TW-SW**	1.59	0.02
64	**RF-SW**	1.59	0.01
65	**RW-TW**	1.55	0.06
66	**RW-RF**	1.53	0.13
67	**TW-TW**	1.53	0.03
68	**KW-RF**	1.52	0.16

69	**TW-QW**	1.49	0.04
70	**WW-KW**	1.47	0.03
71	**RW-KW**	1.47	0.23
72	**YF-KW**	1.46	0.23
73	**RF-VW**	1.45	0.04
74	**WF-KW**	1.43	0.04
75	**KW-TW**	1.41	0.19
76	**RW-VW**	1.39	0.28
77	**KW-VW**	1.38	0.03
78	**KW-G**	0.96	0.02
79	**RF-G**	0.95	0.05
80	**SW-G**	0.95	0.01
81	**QW-G**	0.95	0.00
82	**RW-G**	0.95	0.02
83	**TW-G**	0.95	0.02
84	**IF-G**	0.90	0.00
85	**YF-G**	0.89	0.01
86	**VW-G**	0.89	0.02
87	**LW-G**	0.88	0.01
88	**WF-G**	0.84	0.01
89	**KW-SW**	0.84	0.16
90	**WW-G**	0.83	0.02

Peptide characterisation data

HPLC and MS characterization of the individual monomeric sequences

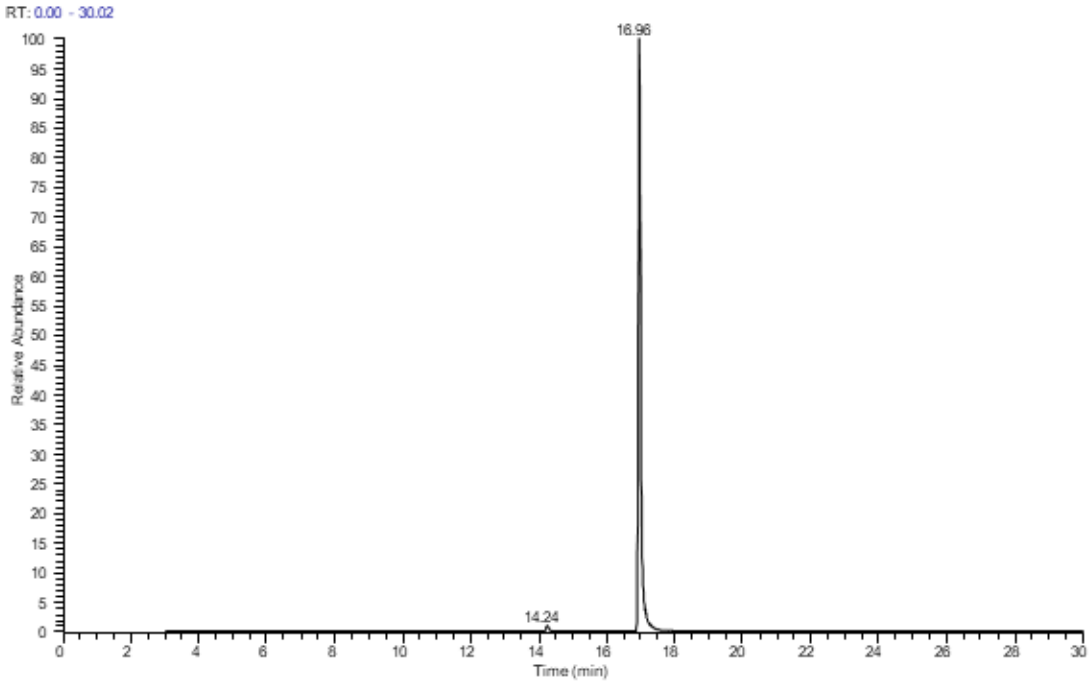

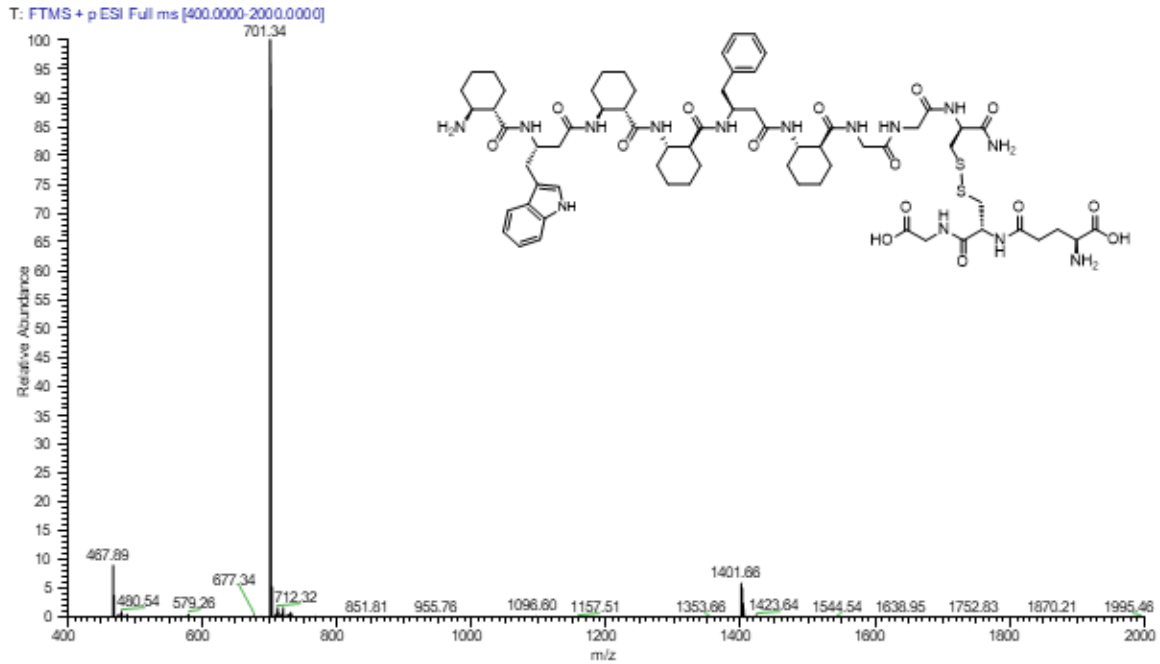

HPLC trace and mass spectrum of the glutathionic precursor **WF-G** (exact mass: 1400.66). Calculated isotopic profile for $[M+2H]^{2+}$ (species, abundance): 701.3383 (100%), 701.8400 (72.47%), 702.3417 (25.86%), 702.8379 (6.48%); m/z calculated: 1401.67 $[M+H]^{+}$, 701.24 $[M+2H]^{2+}$; m/z observed: 1401.06 $[M+H]^{+}$, 701.34 $[M+2H]^{2+}$

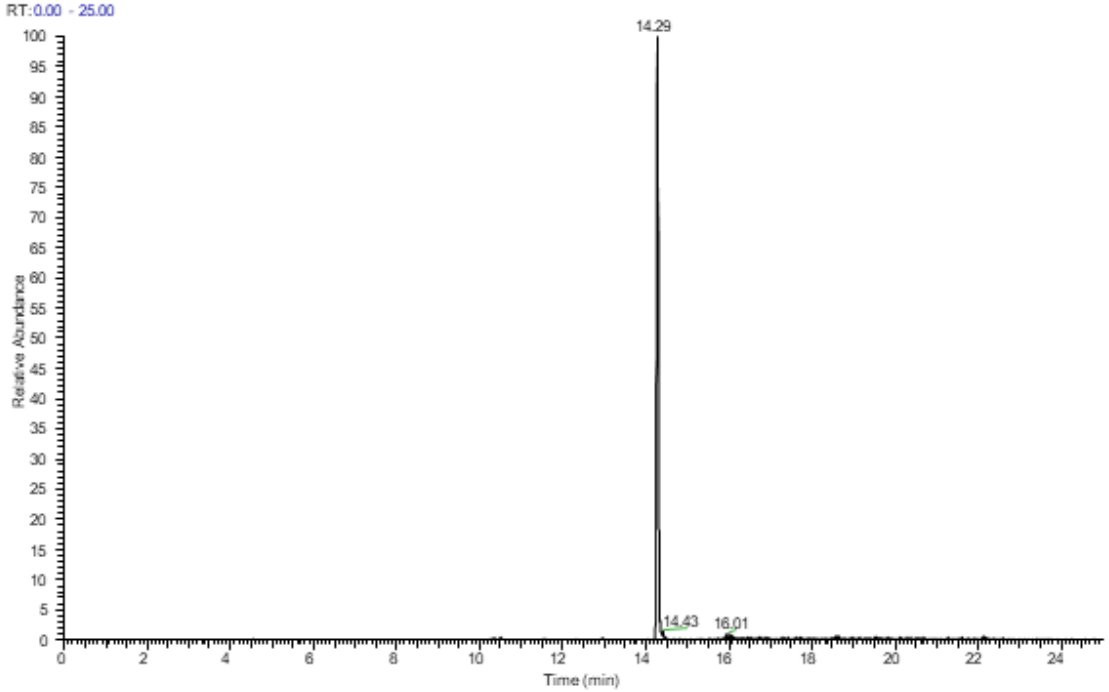

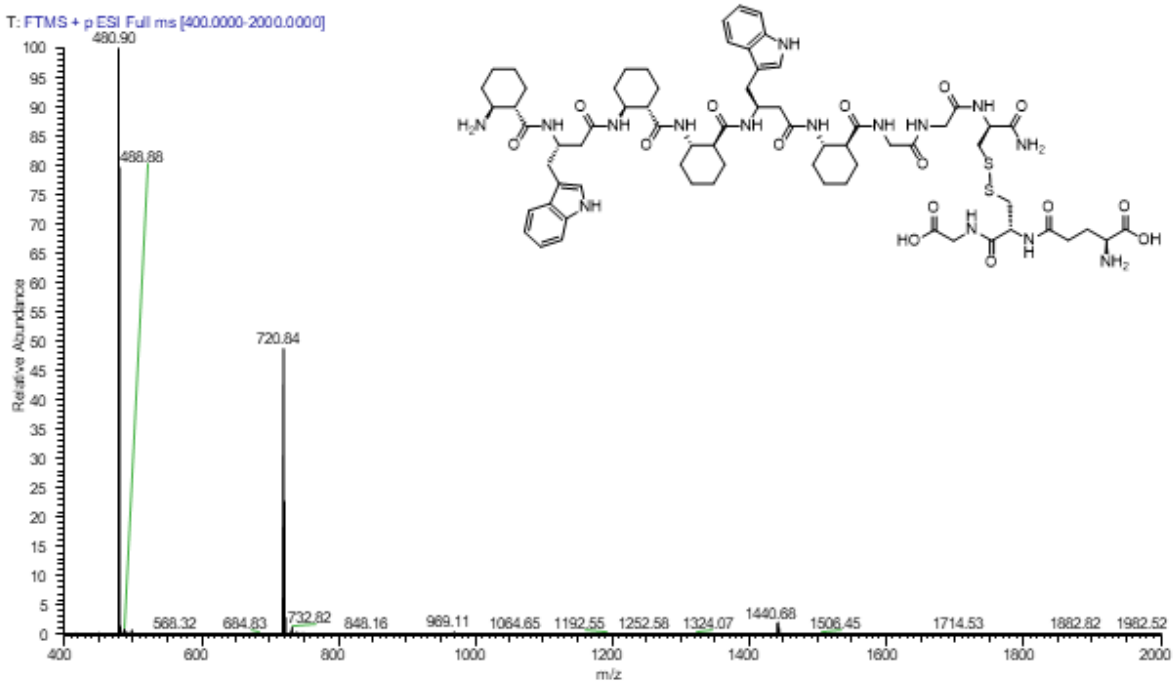

HPLC trace and mass spectrum of the glutathionic precursor **WW-G** (exact mass: 1439.67). Calculated isotopic profile for $[M+2H]^{2+}$ (species, abundance): 720.8438 (100%), 721.3454 (74.63%), 721.8471 (27.44%), 722.3434 (6.78%); m/z calculated: 1440.51 $[M+H]^{+}$, 720.76 $[M+2H]^{2+}$, 480.84 $[M+3H]^{3+}$; m/z observed: 1440.68 $[M+H]^{+}$, 720.64 $[M+2H]^{2+}$, 480.90 $[M+3H]^{3+}$

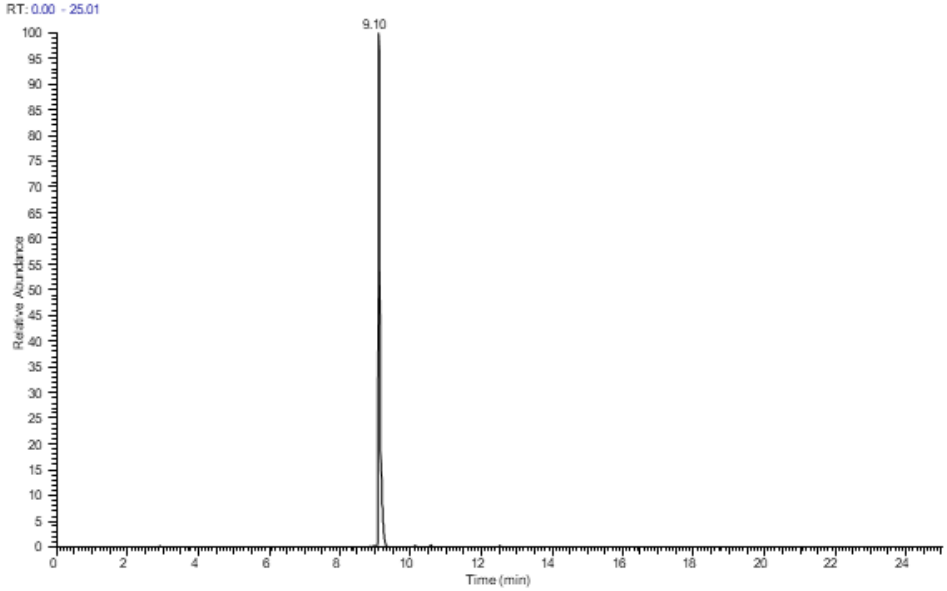

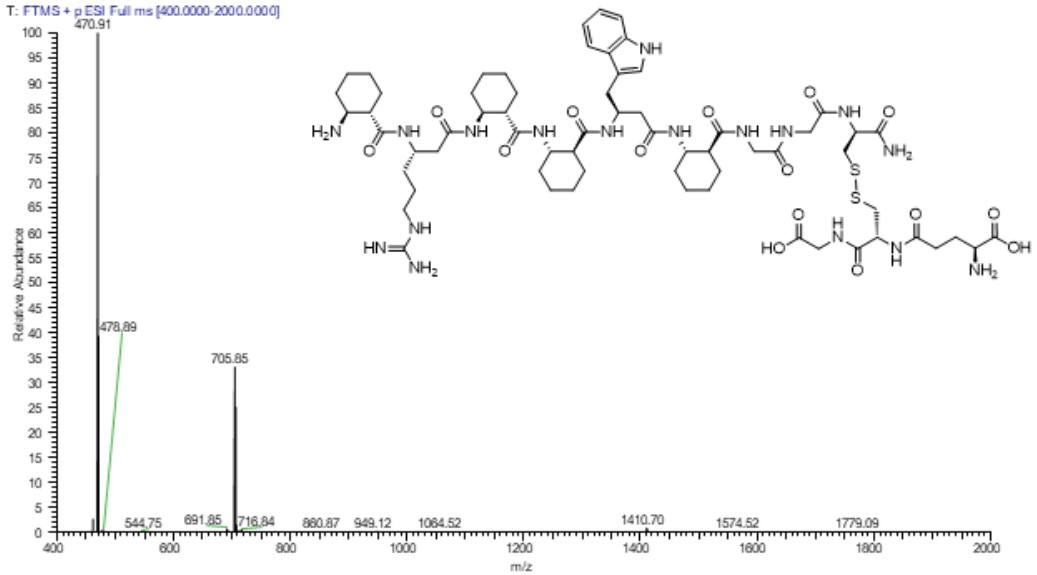

HPLC trace and mass spectrum of the glutathionic precursor **RW-G** (exact mass: 1409.69). Calculated isotopic profile for $[M+2H]^{2+}$ (species, abundance): 705.3508 (100%), 705.8524 (69.22%), 706.3487 (8.95%), 706.3510 (4.30%); m/z calculated: 1410.49 $[M+H]^{+}$, 705.75 $[M+2H]^{2+}$, 470.83 $[M+3H]^{3+}$; m/z observed: 1410.70 $[M+H]^{+}$, 705.85 $[M+2H]^{2+}$, 470.91 $[M+3H]^{3+}$

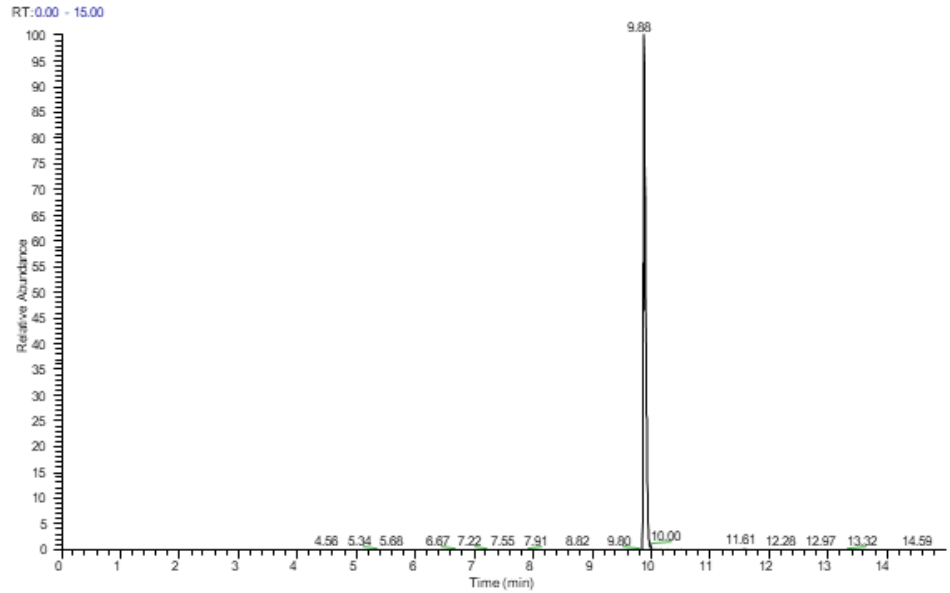

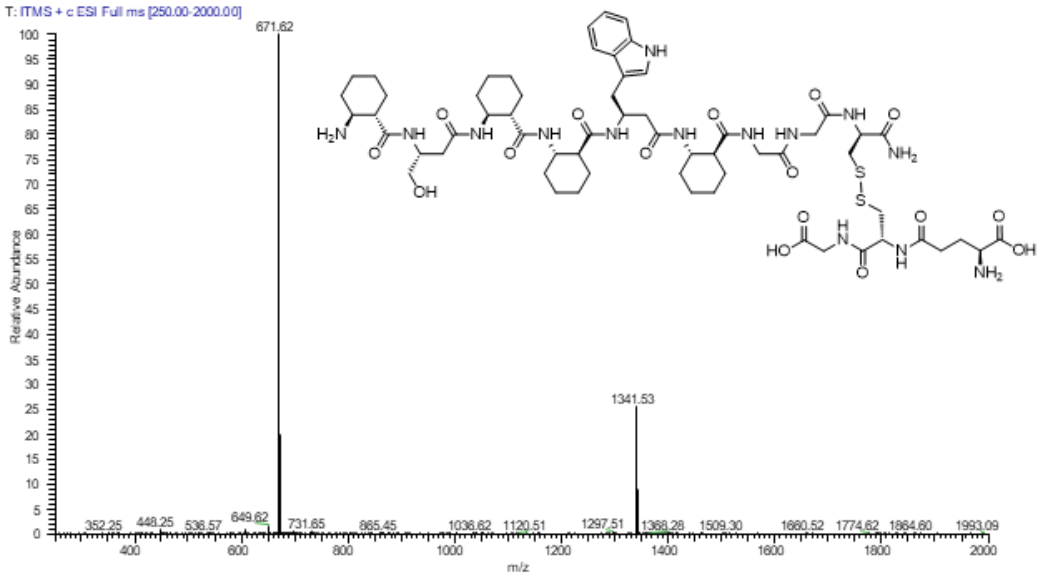

HPLC trace and mass spectrum of the glutathionic precursor **SW-G** (exact mass: 1340.63). Calculated isotopic profile for $[M+2H]^{2+}$ (species, abundance): 670.8162 (100%), 671.3179 (65.98%), 671.8141 (8.95%), 671.8164 (3.37%); m/z calculated: 1341.38 $[M+H]^{+}$, 671.19 $[M+2H]^{2+}$; m/z observed: 1341.53 $[M+H]^{+}$, 671.62 $[M+2H]^{2+}$

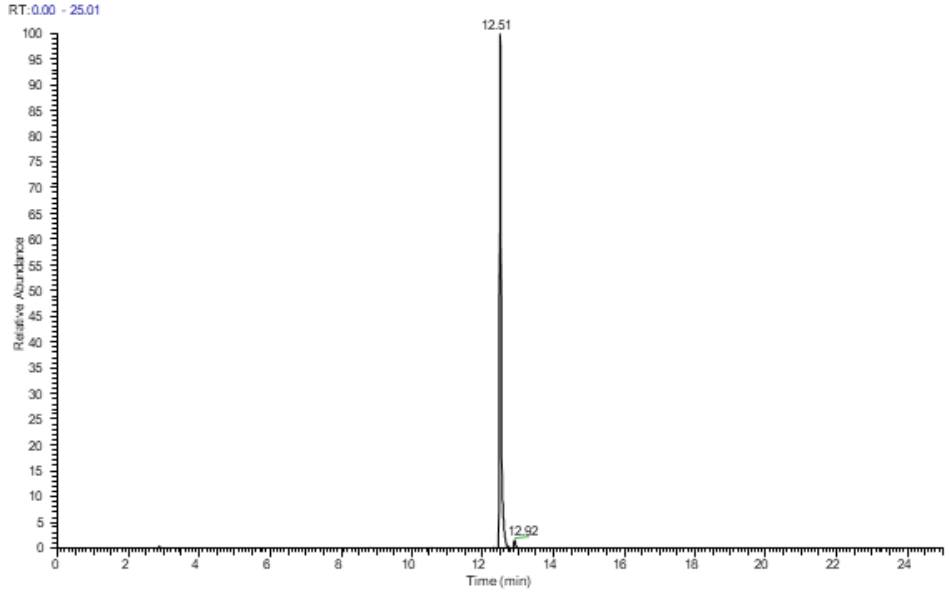

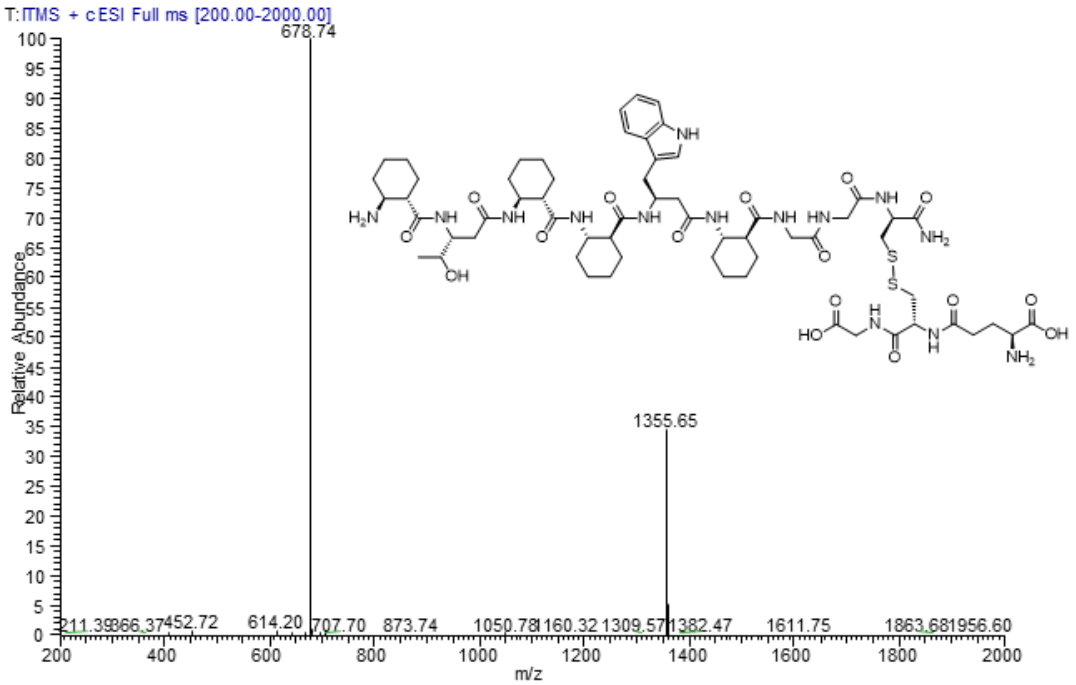

HPLC trace and mass spectrum of the glutathionic precursor **TW-G** (exact mass: 1354.64). Calculated isotopic profile for $[M+2H]^{2+}$ (species, abundance): 677.8240 (100%), 678.3257 (67.06%), 678.8211 (8.95%), 678.8242 (3.43%); m/z calculated: 1355.41 $[M+H]^{+}$, 678.21 $[M+2H]^{2+}$; m/z observed: 1355.65 $[M+H]^{+}$, 678.74 $[M+2H]^{2+}$

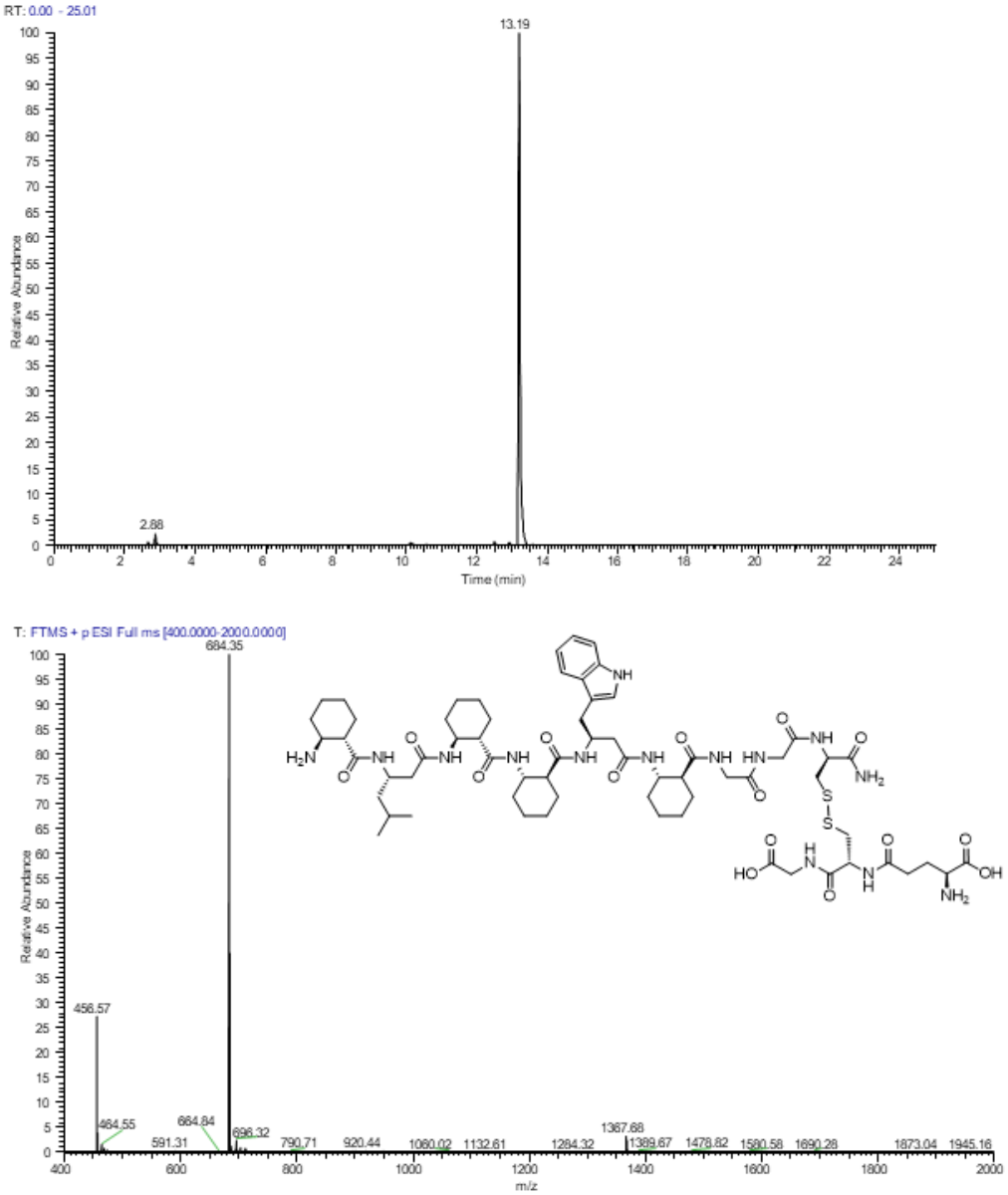

HPLC trace and mass spectrum of the glutathionic precursor **LW-G** (exact mass: 1366.68). Calculated isotopic profile for $[M+2H]^{2+}$ (species, abundance): 683.8422 (100%), 684.3439 (69.22%), 684.8401 (8.95%), 684.8424 (3.54%); m/z calculated: 1367.46 $[M+H]^{+}$, 684.23 $[M+2H]^{2+}$; m/z observed: 1367.68 $[M+H]^{+}$, 684.35 $[M+2H]^{2+}$

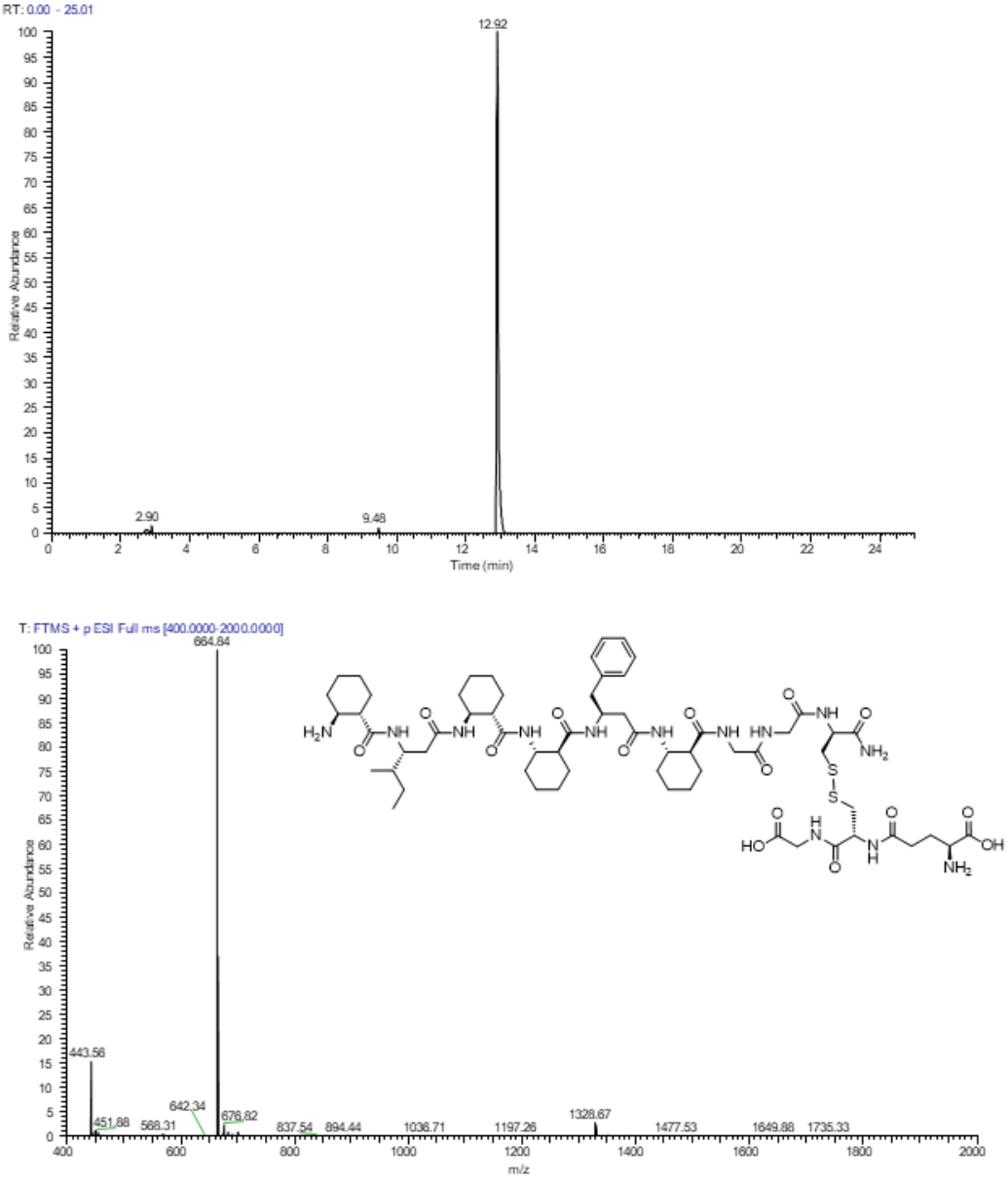

HPLC trace and mass spectrum of the glutathionic precursor **IF-G** (exact mass: 1327.67). Calculated isotopic profile for $[M+2H]^{2+}$ (species, abundance): 664.3468 (100%), 664.8385 (67.06%), 665.3347 (8.95%), 665.3370 (3.18%); m/z calculated: 1328.42 $[M+H]^{+}$, 664.71 $[M+2H]^{2+}$; m/z observed: 1328.67 $[M+H]^{+}$, 664.84 $[M+2H]^{2+}$

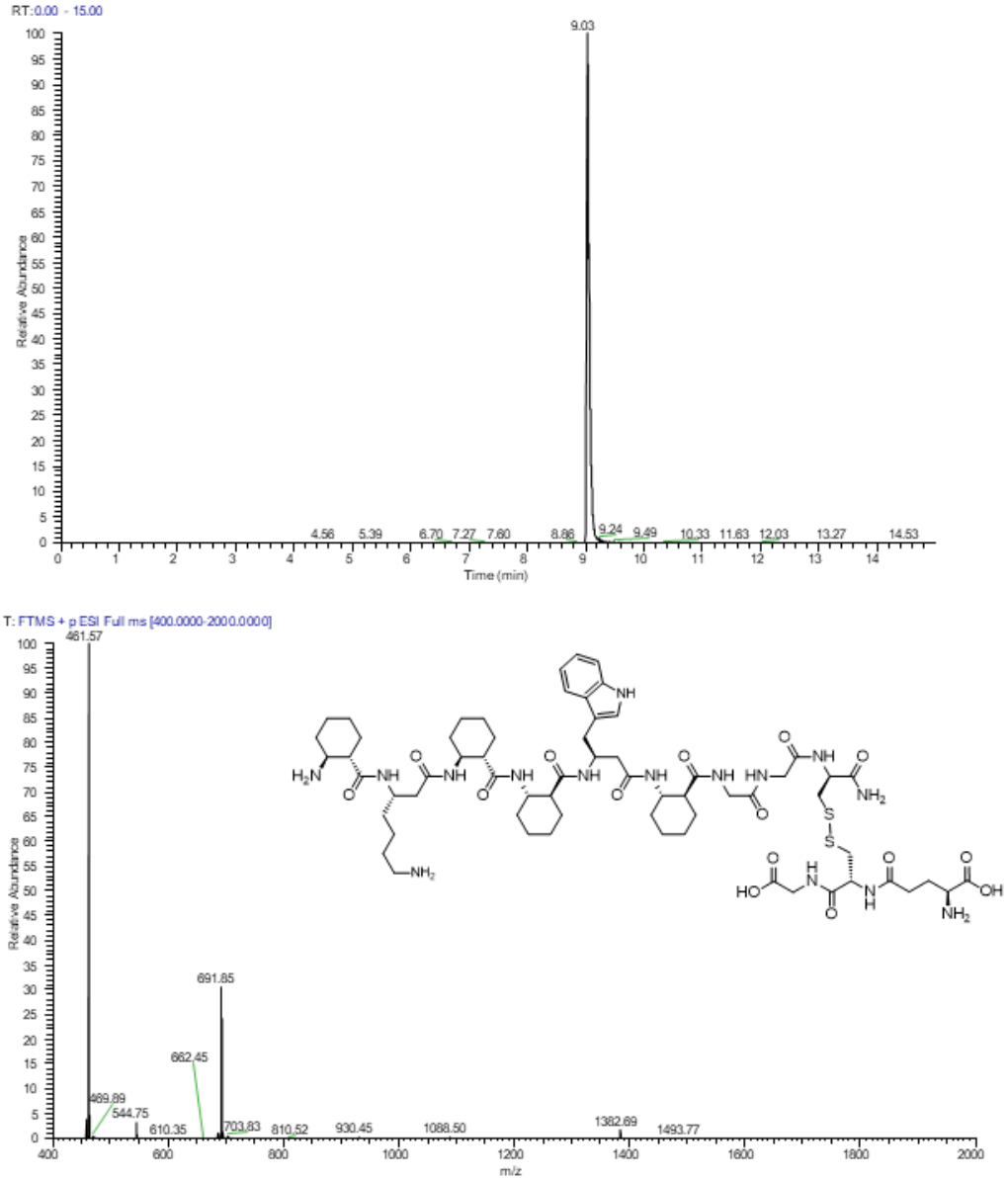

HPLC trace and mass spectrum of the glutathionic precursor **KW-G** (exact mass: 1381.69). Calculated isotopic profile for $[M+2H]^{2+}$ (species, abundance): 691.3477 (100%), 691.8494 (69.22%), 692.3447 (8.95%), 692.3479 (3.79%); m/z calculated: 1382.47 $[M+H]^{+}$, 691.74 $[M+2H]^{2+}$, 461.49 $[M+3H]^{3+}$; m/z observed: 1382.69 $[M+H]^{+}$, 691.85 $[M+2H]^{2+}$, 461.57 $[M+3H]^{3+}$

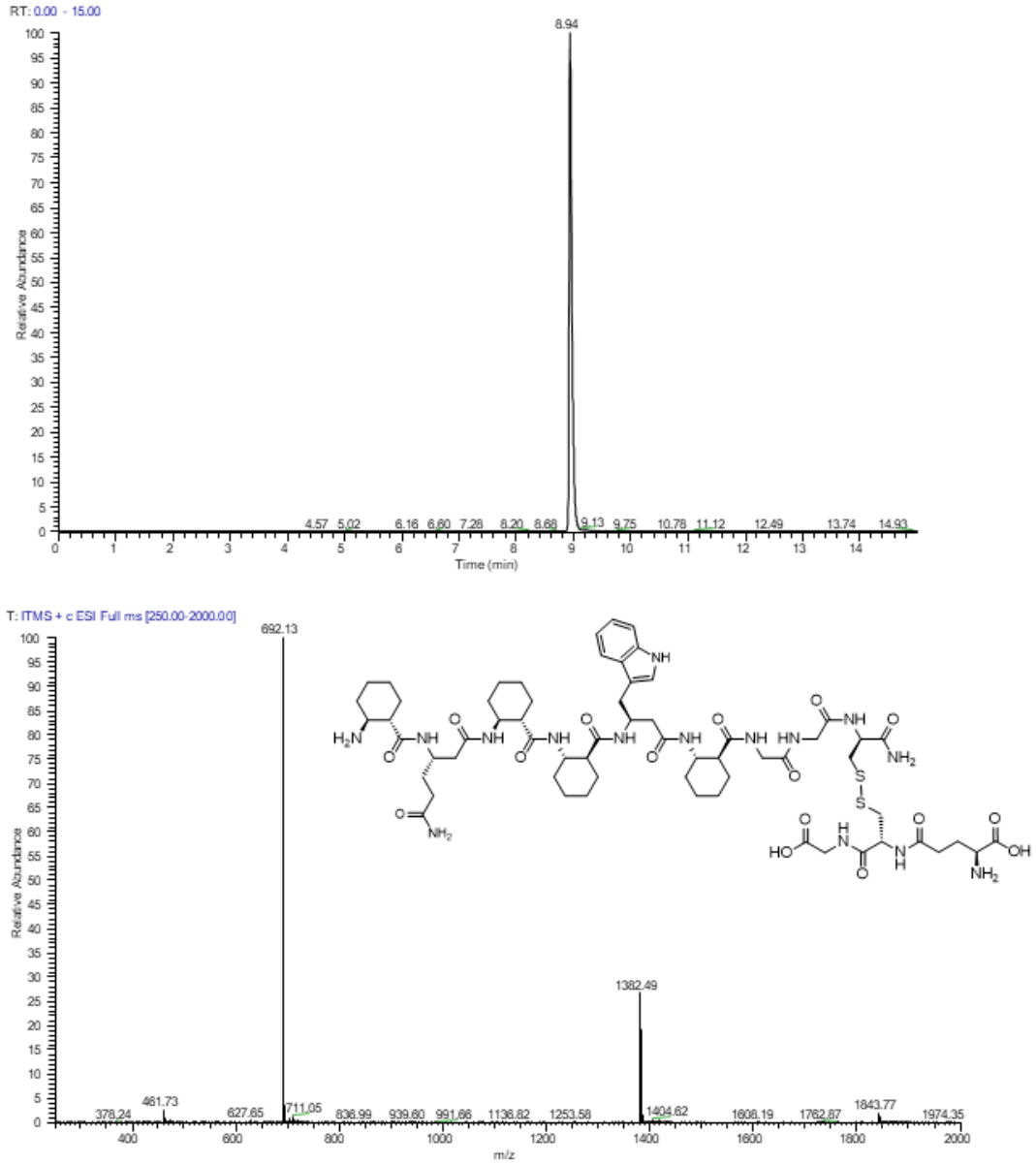

HPLC trace and mass spectrum of the glutathionic precursor **QW-G** (exact mass: 1381.65). Calculated isotopic profile for $[M+2H]^{2+}$ (species, abundance): 691.3295 (100%), 691.8312 (68.14%), 692.3274 (8.95%), 692.3297 (3.73%); m/z calculated: 1382.43 $[M+H]^{+}$, 691.72 $[M+2H]^{2+}$; m/z observed: 1382.49 $[M+H]^{+}$, 692.13 $[M+2H]^{2+}$

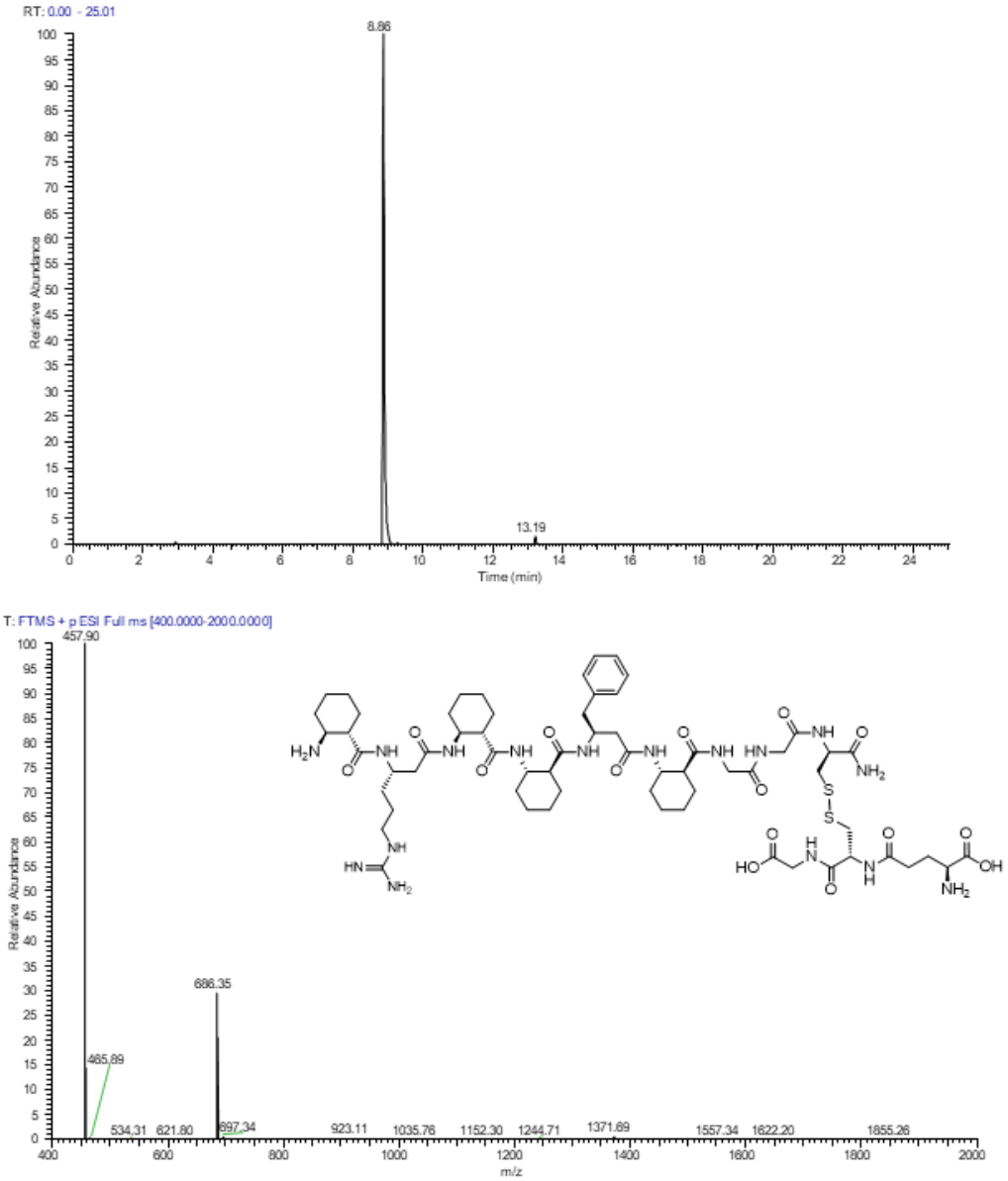

HPLC trace and mass spectrum of the glutathionic precursor **RF-G** (exact mass: 1370.68). Calculated isotopic profile for $[M+2H]^{2+}$ (species, abundance): 685.8453 (100%), 686.3470 (67.06%), 686.8432 (8.95%), 686.8455 (3.92%); m/z calculated: 1371.45 $[M+H]^{+}$, 686.23 $[M+2H]^{2+}$, 457.82 $[M+3H]^{3+}$; m/z observed: 1371.69 $[M+H]^{+}$, 686.35 $[M+2H]^{2+}$, 457.90 $[M+3H]^{3+}$

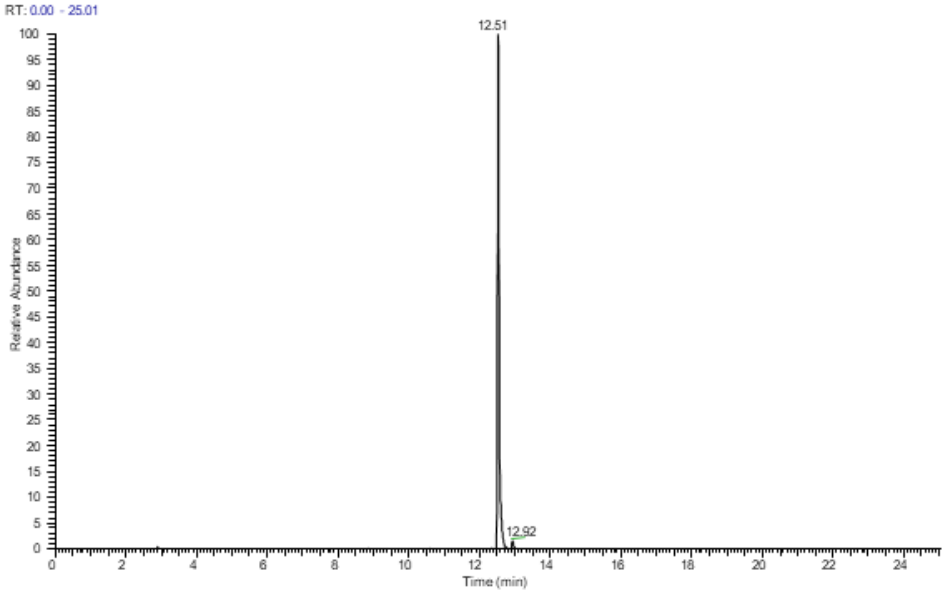

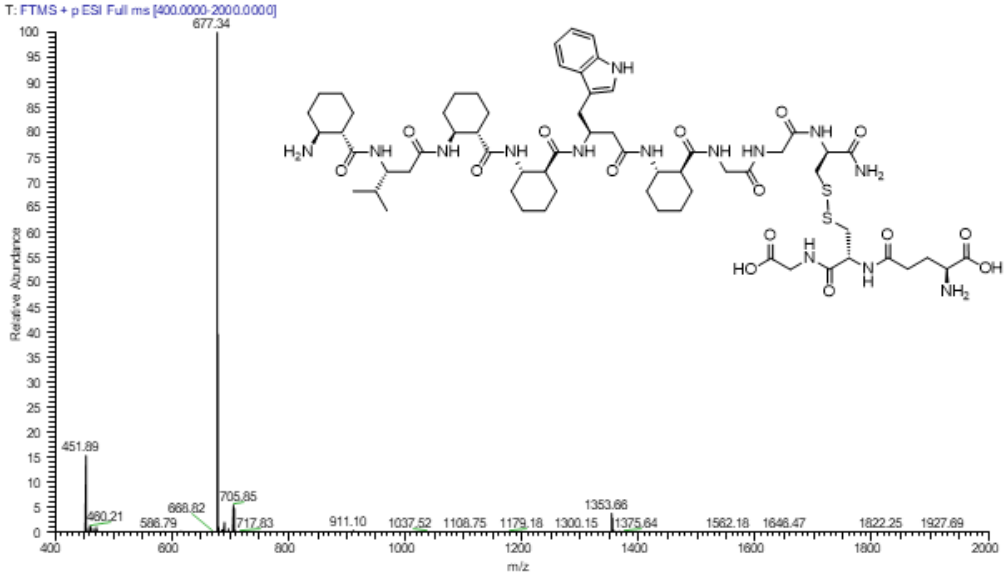

HPLC trace and mass spectrum of the glutathionic precursor **VW-G** (exact mass: 1352.66). Calculated isotopic profile for $[M+2H]^{2+}$ (species, abundance): 676.8344 (100%), 677.3361 (68.14%), 677.8323 (8.95%), 677.8346 (3.49%); m/z calculated: 1353.43 $[M+H]^{+}$, 677.22 $[M+2H]^{2+}$; m/z observed: 1353.66 $[M+H]^{+}$, 677.34 $[M+2H]^{2+}$

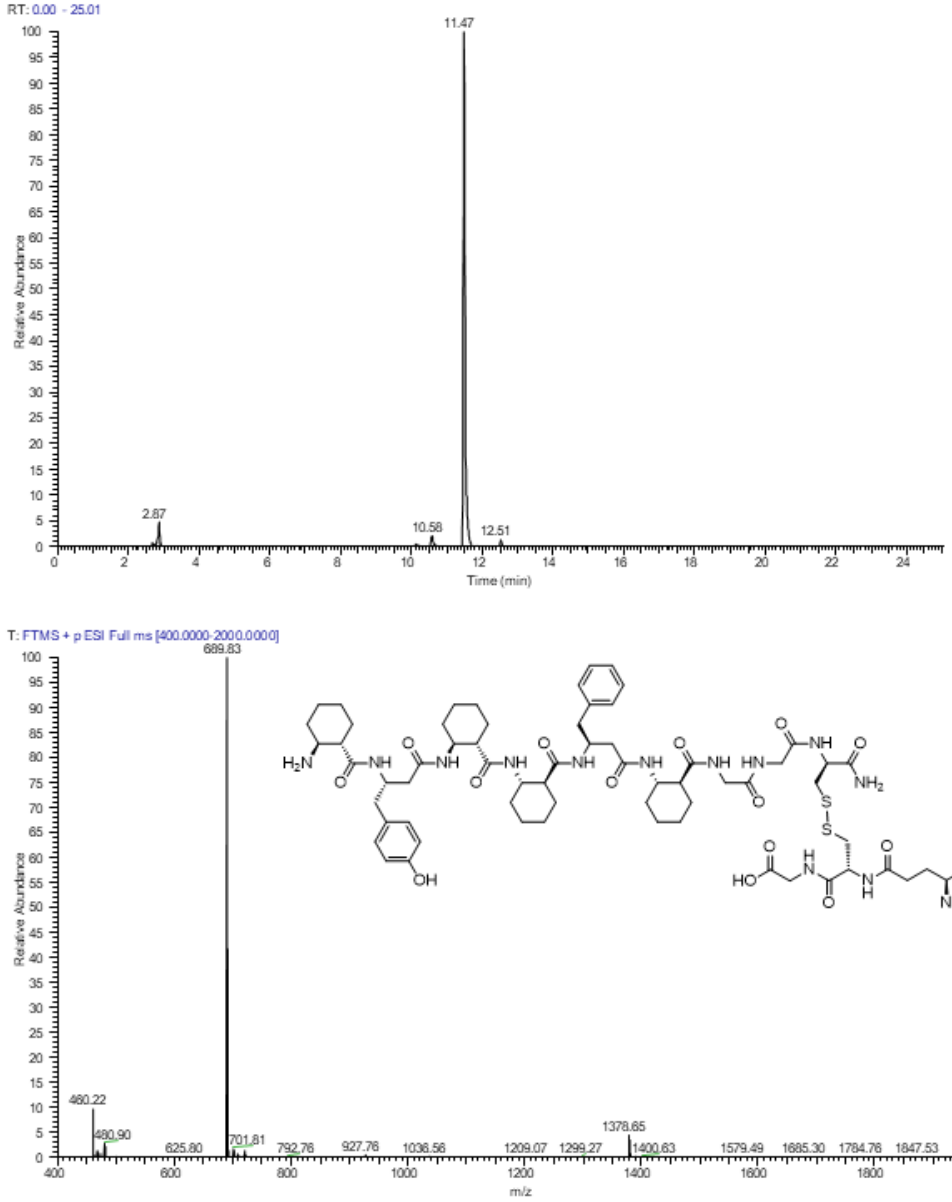

HPLC trace and mass spectrum of the glutathionic precursor **YF-G** (exact mass: 1377.65). Calculated isotopic profile for $[M+2H]^{2+}$ (species, abundance): 689.3264 (100%), 689.8281 (70.30%), 690.3243 (8.95%), 690.3266 (3.34%); m/z calculated: 1378.44 $[M+H]^{+}$, 689.72 $[M+2H]^{2+}$; m/z observed: 1378.65 $[M+H]^{+}$, 689.83 $[M+2H]^{2+}$

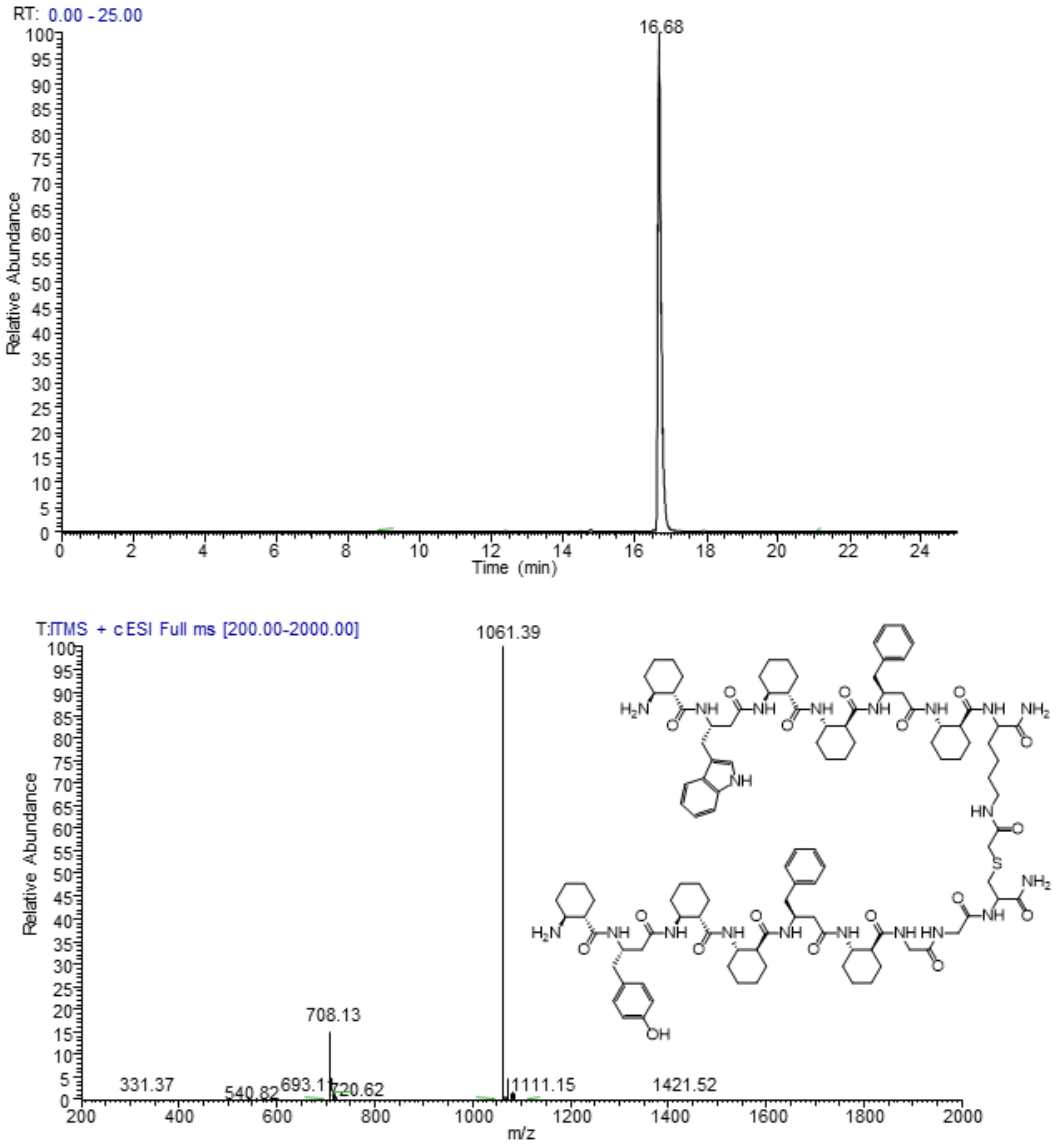

HPLC trace and mass spectrum of the glutathionic precursor **WF-S-YF** (exact mass: 2119.21). Calculated isotopic profile for $[M+2H]^{2+}$ (species, abundance): 1061.1138 (100%), 1060.6121 (81.82%), 1061.6123 (7.31%); m/z calculated: 2120.22 $[M+H]^{+}$, 1061.35 $[M+2H]^{2+}$; 707.90 $[M+3H]^{3+}$ m/z observed: 1061.39 $[M+2H]^{2+}$, 708.13 $[M+3H]^{3+}$

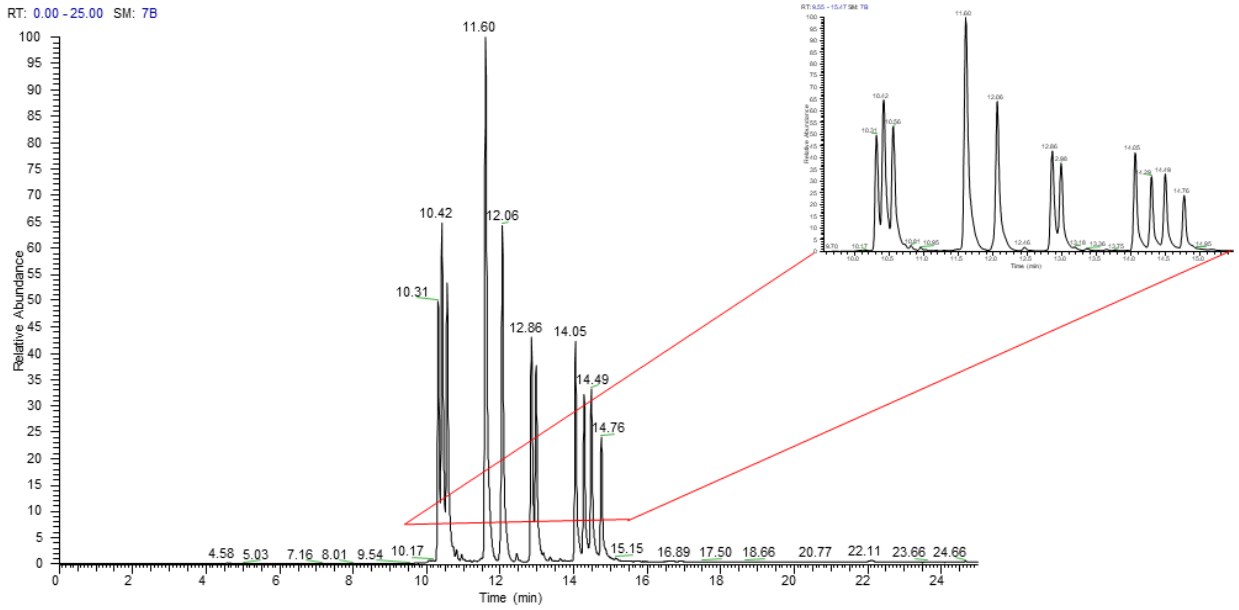

Characterisation of the monomer library. Total ion chromatogram of the initial foldamer library containing 12 different glutathione-protected monomers. Conditions of the analytical HPLC-MS measurement: Column: Aeris Widepore XB-C18 (250 x 4.6 mm) Method: 5–80% B during 25 minutes, flow rate: 0.7 mL min^{-1}, where eluent A: 0.1% HCOOH in water, eluent B: 0.1% HCOOH in ACN. For retention time and molar mass of the compounds, see Table S3.

References

[1] É. Bartus, Z. Hegedüs, E. Wéber, B. Csipak, G. Szakonyi, T. A. Martinek, *ChemistryOpen* **2017**, *6*, 236-241.

[2] A. R. K. Dinesh Gupta, *Can. J. Chem.* **1980**, *58*, 1350-1354.

[3] a) G. von Kiedrowski, in *Bioorganic Chemistry Frontiers* (Eds.: H. Dugas, F. P. Schmidtchen), Springer Berlin Heidelberg, Berlin, Heidelberg, **1993**, pp. 113-146; b) P. G. Higgs, *J. Mol. Evol.* **2017**, *84*, 225-235.

Author Contributions

B.M., Á.B. and É.B. synthesised the foldameric building blocks, performed the dissipative chemical network experiments and analysed the data. A.T. and E.W. analysed the foldamer-foldamer interactions, performed inverse seeding and evaluated the data. G.K. and Z.K. carried out foldamer stability tests. G.F. contributed to the formulation of the concept and wrote the manuscript. T.A.M. developed the concept, designed the experiments, evaluated the experimental results and wrote the manuscript.